

AperTO - Archivio Istituzionale Open Access dell'Università di Torino

Early Oligocene partial melting in the Main Central Thrust Zone (Arun Valley, eastern Nepal Himalaya)

This is the author's manuscript

Original Citation:

Availability:

This version is available <http://hdl.handle.net/2318/128845> since

Terms of use:

Open Access

Anyone can freely access the full text of works made available as "Open Access". Works made available under a Creative Commons license can be used according to the terms and conditions of said license. Use of all other works requires consent of the right holder (author or publisher) if not exempted from copyright protection by the applicable law.

(Article begins on next page)

EARLY OLIGOCENE PARTIAL MELTING IN THE MAIN CENTRAL THRUST ZONE (ARUN VALLEY, EASTERN NEPAL HIMALAYA)

Chiara Groppo^a, Daniela Rubatto^b, Franco Rolfo^{a,c} and Bruno Lombardo^c

a - Dept. of Mineralogical and Petrological Sciences, University of Torino, via Valperga Caluso 35, I-10125, Torino, Italy

b - Research School of Earth Sciences, The Australian National University, Canberra 0200, Australia

c - IGG – CNR, Via Valperga Caluso 35, I-10125, Torino, Italy

* Corresponding author:

Chiara Groppo

Phone: +39 011 6705106

Fax: +39 011 6705128

e-mail: chiara.groppo@unito.it

ABSTRACT

The Main Central Thrust Zone (MCTZ) is a key tectonic feature in the architecture of the Himalayan chain. In the Arun valley of the eastern Nepal Himalaya, the MCTZ is a strongly deformed package of amphibolite- to granulite facies metapelitic schist and granitic orthogneiss. This package is tectonically interposed between the underlying, low-grade, Lesser Himalaya sequences and the overlying, high-grade and locally anatexitic, Higher Himalayan Crystallines (HHC). The MCTZ is characterized by a well documented inverted metamorphism from the Grt-Bt zone, across the Ky-in, St-in and -out, Kfs-in, Ms-out and Sil-in isograds. Partial melting with local occurrence of migmatitic segregations has been rarely reported from the highest structural levels of the MCTZ.

While it is widely accepted that thrusting along the MCT occurred during the Miocene, geochronological data constraining the timing of crustal anatexis in the upper portion of the MCTZ are still lacking. In order to understand the link between partial melting in the MCTZ and the Miocene activation of the MCT, we present the P-T-time evolution of a kyanite-bearing anatexitic gneiss occurring at the highest structural levels of the MCTZ, along the Arun-Makalu transect (Eastern Nepal).

Microstructural observations combined with P-T pseudosection analysis show that dehydration partial melting occurred in the kyanite-field. After reaching peak conditions at about 820°C, 13 kbar, the studied sample experienced decompression accompanied by cooling down to 805°C, 10 kbar, which caused *in situ* melt crystallization. SHRIMP monazite and zircon geochronology provides evidence that the anatexis affecting the upper portion of the MCTZ occurred during Early Oligocene (~31 Ma). These results demonstrate that in the upper MCTZ, at least in the eastern Himalaya, crustal anatexis was earlier than, and not a consequence of, decompression linked to exhumation along the MCT.

Key-words: Main Central Thrust Zone, Himalaya, partial melting, pseudosections, monazite-zircon geochronology

1. Introduction

The Himalayan chain is an exceptional natural laboratory for investigating continental collision processes responsible for the construction of mountain belts. Being one of the most active collisional orogens worldwide, the Himalaya has been the focus of much attention over the last 20 years. The numerous structural and metamorphic studies that are available for different portions of the Eastern Himalaya, from central Nepal to Sikkim–Bhutan rely significantly on the timing of the different deformation and metamorphic events.

Currently available geochronological data that constrain peak metamorphism at different structural levels, including crustal melting and emplacement of leucogranites, mainly refer to central Nepal (e.g. Hodges et al., 1996, 1998; Vannay and Hodges, 1996; Edwards and Harrison, 1997; Coleman, 1998; Coleman and Hodges, 1998; Godin et al., 2001; Kohn et al., 2001, 2005) and the Sikkim-Bhutan region (Daniel et al., 2003; Harris et al., 2004; Catlos et al., 2004), whereas only a few investigate eastern Nepal (Simpson et al., 2000; Viskupic and Hodges, 2001; Viskupic et al., 2005; Jessup et al., 2008). Furthermore, most of these geochronological data refer to the Higher Himalayan Crystallines (HHC) occurring in the structurally higher portion of the Himalayan chain, and only few are related to the underlying Main Central Thrust Zone (MCTZ) (Kohn et al., 2001, 2005; Daniel et al., 2003; Catlos et al., 2004). Altogether, the geochronological and petrological data suggest the existence of two main metamorphic events in the Himalayan evolution: (i) an Eocene-Oligocene metamorphism at HT-HP conditions leading to anatexis and crustal thickening, and (ii) a Miocene thermal event that coincides with movements along the Main Central Thrust, production of the Higher Himalayan leucogranites and onset of the South Tibetan detachment system at higher structural levels (Godin et al., 2001 and references therein).

Geochronological evidence of the HT-HP event is rare and it has been reported only from the HHC because elsewhere it is often obliterated by the pervasive Miocene thermal overprint. As concerning the eastern Himalaya (eastern Nepal, Sikkim and Bhutan), in the Everest region Cottle et al. (2009) recently recognised two phases of metamorphism in a biotite-sillimanite gneiss from the Kangshung Valley: a first Barrovian prograde event at ~39 Ma and a second sillimanite-grade event at ~28 Ma (monazite ages). Simpson et al. (2000) reported monazite growth at 31–32 Ma in equilibrium with the peak metamorphic assemblage garnet + sillimanite + biotite + plagioclase + K-feldspar + quartz; in the same area, a 25–26 Ma monazite age was interpreted by Viskupic and Hodges (2001) as the age of partial melting responsible for the formation of abundant plagioclase + K-feldspar + cordierite leucosomes in sillimanite-bearing orthogneiss.

Leucogranites emplaced in the upper portion of the HHC are significantly younger, showing monazite and xenotime ages of 20–22 Ma in eastern Nepal (Simpson et al., 2000) and 23–22 Ma in Sikkim and Bhutan (e.g. Daniel et al., 2003; Harris et al., 2004; Catlos et al., 2004). Additional melt production occurred at 16–18 Ma (Searle et al., 1997; Viskupic et al., 2005), thus suggesting that Miocene leucogranites represent the products of distinct melting events, protracted from about 26 to 16 Ma (Viskupic et al., 2005).

At lower structural levels, in the MCTZ, geochronological data are scarce and of more complex interpretation. Recently, a diachronous multi-stage metamorphic history has been proposed for the MCTZ on the basis of geochronological data from the Darondi and Langtang Valleys in central Nepal, and from Sikkim and Bhutan. The oldest ages (18–22 Ma, monazite ages) have been reported from the higher structural levels (kyanite-grade) of the MCTZ by Kohn et al. (2001) and Daniel et al. (2003). Monazite ages systematically decrease at progressively lower structural levels through the MCTZ (from staurolite- to garnet-grade), from 16–12 Ma to 8–9 Ma (Kohn et al., 2001,

2005; Catlos et al., 2004). In spite of the still scarce geochronological data available for the MCTZ, its metamorphic evolution is well constrained. The MCTZ is characterized by inverted metamorphism from the garnet-biotite zone, across the staurolite-in, kyanite-in, K-feldspar-in, muscovite-out and sillimanite-in isograds (e.g. Le Fort, 1975; Hodges et al., 1988; Hubbard, 1989; Pêcher, 1989; Inger and Harris, 1992; Meier and Hiltner, 1993; Lombardo et al., 1993; Macfarlane, 1995; Guillot, 1999; Vannay and Hodges, 1996; Fraser et al., 2000; Goscombe and Hand, 2000; Dasgupta et al., 2004). Partial melting with local occurrence of migmatitic segregations has been rarely reported from the highest structural levels of the MCTZ (Hubbard, 1989; Goscombe et al., 2006; Dasgupta et al., 2009; Groppo et al., 2009). P-T conditions of this partial melting event have been recently constrained by Groppo et al. (2009) for a kyanite-bearing anatectic metapelite occurring in Eastern Nepal (east side of the Arun Valley) and by Dasgupta et al. (2009) in Sikkim. Crustal anatexis in the upper portion of the MCTZ differs from the partial melting in the HHC because it occurred at higher pressures, leading to the development of kyanite-bearing assemblages, whereas migmatites from the HHC are generally characterized by lower-P sillimanite \pm cordierite assemblages (e.g. Pognante and Benna, 1993; Goscombe et al., 2006; see also section 7.1). Geochronological data constraining the timing of crustal anatexis in the upper portion of the MCTZ are still lacking.

This paper focuses on the reconstruction of the P-T-time evolution of a garnet-K-feldspar-kyanite anatectic gneiss (AR2) occurring at the highest structural levels of the MCTZ, along the Arun-Makalu transect (Eastern Nepal). Microstructural observations combined with the thermodynamic approach of P-T pseudosections and SHRIMP monazite and zircon geochronology allowed to date the partial melting occurring in the upper portion of the MCTZ. The obtained Early-Oligocene age (\sim 31 Ma) is the oldest age reported for the peak of metamorphism in the MCTZ, and is possibly bound to significantly affect future geodynamical modelling of the Himalayan chain.

2. Geological setting

2.1 Summary of the MCTZ in eastern Nepal

Goscombe et al. (2006) described the crustal architecture of the Himalaya in eastern Nepal as consisting of two main lithotectonic units: the Lesser Himalayan Sequence (LHS) and the Greater Himalayan Sequence (GHS). The LHS and GHS are separated by a stratigraphic unconformity (Himalayan Unconformity, HU), not corresponding to a deformational discontinuity but defined on the basis of lithostratigraphic, isotopic and geochronological data (Goscombe et al., 2006, with references therein).

The same authors define the MCTZ as a strongly deformed package of both LHS and GHS amphibolite-facies metapelitic schist and granitic orthogneiss characterized by a well documented inverted metamorphism and structurally sandwiched between two major deformational and metamorphic discontinuities (cf. their Fig. 3): (i) the Main Central Thrust (MCT) at its bottom, which separates the MCTZ from the underlying Lesser Himalaya units, and (ii) the High Himal Thrust (HHT) at its top, which separates the MCTZ from the overlying high-grade HHC (corresponding to the Upper Plate of Goscombe et al., 2006). In eastern Nepal, the HHT occurs within the GHS, at a structural level higher than the HU, whereas in central and western Nepal it roughly coincides with the HU. As a consequence, the MCTZ has a variable thickness along the Himalayan front (cf. Fig. 2 in Goscombe et al., 2006), ranging from \sim 20 km in eastern Nepal to a few kilometres in central and western Nepal.

Searle et al. (2008) also attempted to find a common definition for the Main Central Thrust in Nepal, mainly using structural criteria. According to these authors, the position of the MCT is approximately the same as in Goscombe et al. (2006); however, they did not discuss the existence of the HHT, considering the anatectic gneisses below and above this structure as part of the same GHS metamorphic package. As a consequence, the MCTZ as defined by Goscombe et al. (2006) has not been recognised by Searle et al. (2008).

Our field and petrologic data are in agreement with the observations of Goscombe et al. (2006): therefore, this paper will follow their structural and metamorphic scheme. It has however to be noted that in other areas of the eastern Himalaya, MCT and MCTZ have been defined differently (e.g. Catlos et al., 2004, Dasgupta et al., 2009) and thus the data presented here are compared to rocks occupying a similar structural level independently of their proposed structural unit.

2.2 Tectonometamorphic units in the Arun Tectonic Window

The valley of the Arun River, flowing in a N-S direction from the Tibetan plateau N and E of the Everest and Makalu massifs to the Terai plain, offers a complete section of the eastern Himalayan nappe pile as it cuts through the Arun Tectonic Window (ATW) (Bordet, 1961 and references therein; Hagen, 1969). The ATW is centred on the Arun antiform (“trans-anticlinal de l’Arun” – Bordet, 1961), a major late-tectonic structure c. 100 km long, and strikes N to NE transversely to the E-W trend of the eastern Himalaya, from the lower Arun valley to beyond the Nepal-China boundary in the upper Arun valley (Fig. 1). From S to N, i.e. from the core of the window structurally upwards in the nappe pile, the tectonic units exposed in the ATW are (Fig.1b):

- (i) the Lesser Himalaya Tumlingtar Unit (Lombardo et al., 1993), a thick sequence of low-grade Upper Precambrian phyllite and quartzite bounded to the N at its top by a thrust zone (Main Central Thrust Zone of Meier and Hiltner, 1993). The Tumlingtar Unit corresponds to the low-grade metasediments defined elsewhere in E Nepal as Seti formation (Shrestha et al., 1984), which are a distinctive component of the upper Lesser Himalaya nappe pile.
- (ii) the Main Central Thrust Zone, consisting of an inverted metamorphic sequence of garnet-biotite-, staurolite-, kyanite- to sillimanite-grade micaschists and granitic orthogneiss (Khandbari Orthogneiss, Andrews, 1985; Num Orthogneiss, Lombardo et al., 1993), lying on top of the Tumlingtar Unit. The MCTZ was formerly called Lesser Himalayan Crystalline by Lombardo et al. (1993), basing on the hypothesis that it could represent a coherent tectonic unit. Recent petrological studies (Goscombe et al., 2006; Groppo et al., 2009), however, have shown that different metamorphic packages, characterized by different P-T evolutions and T/depth ratios and separated by transitional, often cryptic, metamorphic discontinuities, are superposed within the MCTZ.
- (iii) the Higher Himalayan Crystalline nappe (Tibetan Slab of Bordet, 1977) bounded at its bottom, on both sides of the ATW, by thrust sheets defining a major synmetamorphic thrust (High Himal Thrust - HHT - of Goscombe et al., 2006, formerly noted as Main Central Thrust by Bordet, 1961 and Lombardo et al., 1993).

2.3 The Arun-Makalu transect

In the transect from the Arun valley, W of Num, to Makalu through the Barun valley (Brunel and Kienast, 1986; Pognante and Benna, 1993; Goscombe and Hand, 2000), the MCTZ is a complex sequence of Barrovian metamorphic rocks bounded at the top by a belt of thrust sheets (Bordet, 1961; Lombardo et al., 1993) (Fig. 1c) that are roughly coincident with the HHT as defined by

Goscombe et al. (2006). Metamorphic grade increases up section from garnet-biotite zone at the bottom (Arun River) to staurolite- (Tashigaon), kyanite- and sillimanite-K-feldspar zones (above Tashigaon) (e.g. Pognante and Benna, 1993; Goscombe and Hand, 2000). Partial melting with local occurrence of migmatitic segregations has been reported from the highest structural levels of the MCTZ by Goscombe et al. (2006).

A belt of metasedimentary and metagranitic thrust sheets, approximately coincident with the HHT as defined by Goscombe et al. (2006), separates the MCTZ from the overlying HHC. The metasedimentary rocks of the thrust sheets are garnet-kyanite-biotite-muscovite micaschists and gneisses with calcisilicate rocks. The metagranitic thrust sheets are associated with garnet amphibolites, some of which are anthophyllite/gedrite amphibolites that record decompression from higher P and lower T assemblages (anthophyllite/gedrite+kyanite) to lower P and higher T assemblages (garnet+cordierite) (Lombardo et al., 1998). The lower part of HHC is a 6–7 km thick sequence in which upper amphibolite- to medium-P granulite-facies metasediments (Barun Gneiss; Bordet, 1961; Brunel and Kienast, 1986; Lombardo et al., 1993; Pognante and Benna, 1993; Goscombe et al., 2006) are associated with large tabular bodies of granitic orthogneisses (Namche Migmatite Orthogneiss; Lombardo et al., 1993). The granite protolith is Early Paleozoic (Ferrara et al., 1983; Tonarini et al., 1994; Viskupic et al., 2005). Both the metasediments and the orthogneisses display evidence of medium- to low-P partial melting due to hydrate-minerals breakdown and are characterized by sillimanite \pm cordierite assemblages.

The upper part of the HHC in the Barun valley consists of biotite paragneisses and micaschists (Black Gneiss; Bordet, 1961). These metamorphic rocks host networks and lens-shaped bodies of two-micas and tourmaline-bearing leucogranites, which can be as thick as 1-2 km (Makalu, Baruntse). Both leucogranite types were produced by partial melting under LP/HT conditions ($P \approx 3\text{--}3.5$ kbar, $T \approx 640\text{--}700^\circ\text{C}$) in the andalusite–sillimanite stability field; the prograde character of leucogranite melt-producing reactions in the Everest–Makalu area suggests that the generation of Miocene leucogranites took place in a regime of nearly isobaric heating following nearly isothermal decompression (Visonà and Lombardo, 2002).

Further up in the sequence, the top of the HHC coincides with the muscovite-in isograd and appears as a major intracrustal detachment zone (South Tibetan Detachment System, STDS, Burchfiel et al., 1992), which brought the HHC into contact with the low-grade metasediments at the base of the Tethyan Zone (North Col Formation) and Ordovician limestones during the Miocene. Meso- and microstructural investigations in different regions (Mt. Everest: Carosi et al., 1998; Searle, 1999; Searle et al., 2003; Bhutan: Grujic et al., 1996; Annapurna-Manaslu: Searle and Godin, 2003) revealed that the STDS comprises two discrete detachments, one ductile and one fragile.

2.3 Kyanite-bearing migmatites at the top of MCTZ

The structurally highest portion of the MCTZ along the Arun-Makalu transect is poorly exposed and outcrops are mainly limited to creek beds within a dense forest. The sample studied in this paper was collected from an outcrop located in the second creek above the village of Tashigaon, just below Dahara Kharka (Fig. 1c). The outcrop consists of a medium-grained, garnet-biotite gneiss with elongated, centimetres-thick, quartzo-feldspathic lenses and pods parallel to the main foliation, which dips about 40° to the NW.

3. Methods

The rock-forming minerals were analysed with a Cambridge Stereoscan 360 SEM equipped with an EDS Energy 200 and a Pentafet detector (Oxford Instruments) at the Department of Mineralogical and Petrological Sciences, University of Torino. The operating conditions were: 50 seconds counting time and 15 kV accelerating voltage. SEM-EDS quantitative data (spot size = 2 μ m) were acquired and processed using the Microanalysis Suite Issue 12, INCA Suite version 4.01; natural mineral standards were used to calibrate the raw data; the $\Phi\rho Z$ correction (Pouchou and Pichoir, 1988) was applied.

Trace element analyses of garnet and monazite were performed by laser ablation – ICP-MS at the Research school of Earth Science, The Australian National University. A pulsed 193 nm ArF Excimer laser with 100 or 70 mJ energy and a repetition rate of 5 Hz (Eggins et al. 1998), coupled to an Agilent 7500 quadrupole ICP-MS were used. During the time-resolved analysis of minerals, the contamination from inclusions, fractures and zones of varying compositions was detected by monitoring several elements. A spot size of 40 μ m for monazite and 70 or 112 μ m for garnet were used. External calibration was performed relative to NIST 612 glass, at the concentrations given in Pearce et al. (1997). Internal standards were Ca and Si for garnet and Ca for monazite, as measured by electron microprobe.

The bulk rock composition of sample AR2 for the thermodynamical modelling was calculated by combining the mineral proportions obtained from the image analysis of the thin section with mineral chemistry acquired at SEM-EDS (Table 1). More in detail, image analysis (software Scion Image, Scion Corporation, Frederick, Maryland) was used to measure the modal proportions of biotite, garnet and kyanite, whereas those of quartz and feldspars were estimated as Qtz:Kfs:Pl=4:3:2 by visual estimate. This bulk composition is comparable with that calculated using the ICP-MS analysis by ALS Chemex, Vancouver, Canada (see Table 2b) and was preferred because the precise estimate of the biotite modal percentage is required to derive the H₂O content in the bulk. H₂O was derived from the modal proportion of biotite and using the biotite Ti-H substitution scheme of White et al., 2007.

Zircon and monazite for the geochronological study were separated from sample AR2 with conventional magnetic and heavy liquid methods. Grains were mounted in epoxy and polished down to expose the grain centres. Cathodoluminescence (CL) and back-scattered electron (BSE) images of zircon and monazite, respectively, were carried out at the Electron Microscope Unit, The Australian National University. The CL investigation was performed with a HITACHI S2250-N scanning electron microscope working at 15 kV, ~60 μ A and ~20 mm working distance. BSE images of monazite were obtained with a Cambridge S360 scanning electron microscope using a voltage of 20 kV, current of 2 nA and a working distance of 17 mm.

U-Th-Pb analyses were performed using a sensitive, high-resolution ion microprobe (SHRIMP II) at the Research School of Earth Sciences. Instrumental conditions and data acquisition were generally as described by Williams (1998). The data were collected in sets of six scans throughout the masses. The measured $^{206}\text{Pb}/^{238}\text{U}$ ratio was corrected using reference zircon (TEM, 417 Ma, Black et al. 2003) and Thompson Mine monazite (1766 Ma, Paces and Miller, 1993). Calibration errors were 1.9% (2 σ) for zircon and 1.6 for monazite. For monazite, energy filtering was applied to eliminate the interference on ^{204}Pb (Rubatto et al., 2001) and reduce any potential matrix effect. Zircon and monazite data were corrected for common Pb on the basis of the measured ^{204}Pb as described in Williams (1998). Common Pb corrections for the analyses yielding Eocene ages using

the measured $^{207}\text{Pb}/^{206}\text{Pb}$ ratio (Williams, 1998) returned identical results. U concentration in zircon was standardised to SL 13 zircon, which contains 238 ppm of U. Age calculation was done using the software Isoplot/Ex (Ludwig, 2003) and assuming the common Pb composition predicted by Stacey and Kramers (1975).

4. Petrography and mineral chemistry

4.1 Microstructure

The studied sample shows a gneissic structure and mainly consists of quartz, K-feldspar, plagioclase, biotite, garnet, minor kyanite, very rare prismatic sillimanite and accessory rutile, monazite, apatite and zircon. Two different domains have been recognised (Fig. 2):

- (i) Fine-grained, biotite-rich, domains (representing ~ 10 vol% of the whole sample): in these mm-thick layers biotite is weakly oriented and defines a discontinuous foliation (Fig. 2a-c). It is always associated with fine-grained plagioclase (Fig. 2f), minor K-feldspar and rare prismatic sillimanite partially overgrowing biotite (Fig. 3a).
- (ii) Coarse-grained domains: they consist of variably re-crystallized quartz ribbons, K-feldspar porphyroblasts (Fig. 2c), minor large crystals of antiperthitic plagioclase (Fig. 2e), kyanite (up to 3-4 mm in length, Fig. 2a-c-g) and garnet (Fig. 2a-b). Minor biotite is preserved as oriented inclusions in quartz ribbons (Fig. 2c), in both plagioclase and K-feldspar porphyroblasts and, more rarely, in kyanite (Fig. 2f). The coarse-grained domains are partially corroded by the fine-grained, biotite-rich layers, according to the following observations: (a) K-feldspar porphyroblasts are corroded by myrmekites and biotite + quartz intergrowths (Fig. 2d), (b) the large antiperthitic plagioclases are partially replaced by finer grained plagioclase of the matrix (Fig. 2e); (c) large garnet porphyroblasts (up to 5 mm in diameter) are partially replaced by plagioclase + biotite intergrowths (Fig. 2b-i-l); (d) large kyanite crystals are partly corroded by plagioclase + biotite \pm K-feldspar aggregates only when they are in contact with the fine-grained matrix (Fig. 2g).

Rutile, apatite, monazite and zircon occur as accessory phases. Zircon is abundant both in the fine-grained biotite-rich domains (Fig. 3b) and in garnet; monazite is mainly interstitial in the fine-grained biotite-rich domains (Fig. 3a) and, when included in garnet, it is only present at the garnet rim (Fig. 2b). Monazite contains small (~5 μm) composite inclusions consisting of biotite, muscovite, quartz, and K-feldspar which may represent former melts (see in the discussion, section 7.2), and suggest that this accessory mineral grew in equilibrium with a quartz + feldspar + biotite melt-bearing assemblage.

4.2 Mineral chemistry

Garnet porphyroblasts are strongly zoned (Fig. 4): the Ca content is low in the core [$X_{\text{Ca}}=0.05-0.06$; $X_{\text{Ca}}=\text{Ca}/(\text{Ca}+\text{Mg}+\text{Fe})$], sharply increases in a Ca-rich annulus ($X_{\text{Ca}}=0.14-0.15$) and then sharply decreases in the rim ($X_{\text{Ca}}=0.08-0.09$). A steep decrease in X_{Ca} ($X_{\text{Ca}}=0.03-0.04$) occurs at the outermost rim. The Fe/(Fe+Mg) ratio (X_{Fe}) progressively increases from 0.74-0.75 in the core to 0.78-0.79 in the outermost rim (Fig. 4 and Table 1). Mn content is low and constant ($X_{\text{Mn}}=0.02-0.04$) throughout the garnet porphyroblasts. Small relicts of garnet preserved in the biotite + plagioclase intergrowths are enriched in both Mn and Fe ($X_{\text{Mn}}=0.05-0.06$; $X_{\text{Fe}}=0.80-0.83$), and show a lower $X_{\text{Ca}}=0.03-0.05$.

Phosphorous concentration is low (47-51 ppm) in both garnet core and Ca-rich annulus, whereas it sharply increases toward the rim (105-203 ppm) (Fig. 4 and Table A available as

background dataset). Ti and Y generally increase from core to the Ca-rich annulus (Ti=90→170 ppm; Y=600→1250 ppm) and sharply decrease toward the rim (Ti=75-90 ppm; Y=300-500 ppm) (Fig. 4). REE patterns for all domains (Fig. 5) show a depletion in LREE, a marked Eu negative anomaly but vary significantly in mid- to heavy-REE. The core has a flat to slightly concave HREE pattern at 200-600 times chondrite; the Ca-rich annulus partly overlaps with the core but also has the most enriched patterns at 900 times chondrite and slightly concave patterns with Yb ~200 times chondrite; the rim is distinct in having the lowest HREE concentrations and concave patterns with Yb down to 75 times chondrite.

Biotite flakes occurring in the fine-grained layers and in the biotite + plagioclase intergrowths are characterized by significantly different X_{Fe} and Ti contents. Biotite in the fine-grained layers has X_{Fe} =0.49-0.52 and Ti=0.24-0.27 a.p.f.u., whereas biotite in the intergrowths has lower X_{Fe} (0.40-0.49) and Ti contents (0.15-0.23 a.p.f.u.) (Table 1). *Plagioclase* occurs in three different microstructural positions, namely as: (i) large porphyroblasts in the coarse-grained domains (Fig. 2e), (ii) finer-grained crystals in the biotite-rich fine-grained layers (Fig. 2f), and (iii) in the biotite + plagioclase intergrowths developed at the garnet rims (Fig. 2i-l). The composition of plagioclase in these microstructural positions is significantly different: the large, antiperthitic plagioclase has lower Ca (X_{Ca} =0.23-0.24) and always contains some K (X_{Or} =0.02-0.03), plagioclase in the fine-grained layers shows X_{Ca} =0.24-0.26, whereas plagioclase in the intergrowths is the richest in Ca (X_{Ca} =0.26-0.27) (Table 1). *K-feldspar* is slightly variable in composition, with albite content ranging from 0.15-0.21 (large porphyroblasts in the coarse-grained domains, Fig. 2c) to 0.08-0.17 (in the fine-grained layers) (Table 1).

4.3 Microstructural evidence of partial melting

Microstructural evidence suggests that the studied rock underwent dehydration partial melting:

- (i) The presence of coarse-grained quartz-feldspathic layers and elongated pods partially corroded by the fine-grained biotite-rich matrix (Fig. 2a-c) is suggestive of residual quartz and feldspars (K-feldspar and plagioclase porphyroblasts) corroded by former melt, finally crystallized as biotite + plagioclase aggregates (see also Indares et al., 2008 and Guilmette et al., pers. com.). Biotite flakes included in restitic quartz and feldspars (Fig. 2c) also escaped anatexis. Kyanite mainly occurs in the coarse-grained domains (Fig. 2a); however, there is no clear evidence of its growth during partial melting (e.g. inclusions of K-feldspar, see Guilmette et al., pers. com.), and it can thus be interpreted either as a residuum or as a peritectic phase.
- (ii) The presence of lobate inclusions of quartz in garnet core (Fig. 2b) has been inferred by Waters (2001) to be indicative of garnet growth via a partial melting reaction: as a consequence, garnet has been interpreted as a peritectic phase;
- (iii) Textures consistent with pseudomorphing of liquid-filled pores (e.g. Holness & Clemens, 1999; Holness & Sawyer, 2008) are locally present, such as thin films of K-feldspar with low dihedral angles against refractory solids (Fig. 2h);
- (iv) Biotite + quartz intergrowths are developed at the expenses of K-feldspar, and biotite + plagioclase intergrowths are present at the rim of porphyroblastic garnet (Fig. 2i-l). Similar microstructures in pelitic granulites have been interpreted as consistent with the final stages of back-reactions involving melt crystallization (e.g. Waters, 2001; Cenki et al., 2002; Álvarez-Valero and Kriegsman, 2010).

The presence of microstructures consistent with the crystallization of a trapped melt (i.e. intergrowths related to back reactions, pseudomorphs of liquid-filled pores) indicates that melt was not completely extracted from the rock. However, the preservation of the HT granulitic assemblage K-feldspar + garnet + kyanite and the absence of muscovite suggest that a substantial proportion of the produced melt was removed from the sites of melting (e.g. White and Powell, 2002; Guilmette et al., pers. com.).

5. Results: modelling of metamorphic evolution

The successful application of conventional thermobarometry to high grade, partially melted rocks is limited by the extensive resetting of garnet and biotite compositions during cooling, and by the fact that most or even all the biotite may be a retrogression product. Recent improvements in thermodynamic databases, melt and solid solution models (White et al., 2007) and in the development of methods for taking into account possible melt loss during the rock evolution (White and Powell, 2002; White et al., 2004, 2007; Halpin et al., 2007), suggest that P-T pseudosections are the most suitable approach to constrain the P-T evolution of anatectic rocks (e.g. Indares et al., 2008; Powell and Holland, 2008).

Sample AR2 was modelled in the model system NCKFMASH; Fe^{+3} was neglected because Fe^{+3} -rich oxides are lacking and the amount of Fe^{+3} in the analysed minerals is very low. The spessartine content in garnet is homogeneous and lower than 4 mol%, therefore a Mn-free system has been considered. Pseudosections have been calculated following the approach of Connolly (1990, 2009) and using the internally consistent thermodynamic dataset and equation of state for H_2O of Holland and Powell (1998, revised 2004). The minerals considered in the calculation were: garnet, biotite, white mica, plagioclase, K-feldspar, cordierite, anhydrous Al-silicates, orthopyroxene, quartz, rutile and ilmenite. The following solid solution models were used: phengite and cordierite (Holland and Powell, 1998), garnet (White et al., 2000), Ti-biotite (White et al., 2007), plagioclase (Newton et al., 1980), K-feldspar (Waldbaum and Thompson, 1969), orthopyroxene (Powell and Holland, 1999) and silicate-melt (Holland and Powell, 2001; White et al., 2001). The fluid was considered as pure H_2O ($a_{\text{H}_2\text{O}}=1$).

The modelled modal proportions of each phase have been used to check the consistency between the pseudosection and the observed mineral assemblage, which corresponds to the mineral assemblage present during final melt crystallization (i.e. at the *solidus*) (e.g. Indares et al., 2008; Guilmette et al., pers. com.). The garnet zoning offers further information on the P-T evolution of sample AR2. Ca zoning similar to that observed in the studied sample has been reported from other high-T metamorphic terranes (e.g. Spear et al., 1990; Kohn et al., 1997; Spear et al., 1999; Indares et al., 2008) and has been inferred to represent a preserved growth zoning, due to the slow diffusivity of Ca in garnet. The steep decrease in X_{Ca} observed at the outermost garnet rim is likely due to retrograde net transfer reactions, and because in anatectic rocks net transfer reactions usually end when melt solidifies, the X_{Ca} of the outermost rim likely represents the conditions of melt crystallization. On the contrary, the uniform $\text{Fe}/(\text{Fe}+\text{Mg})$ ratio (X_{Fe}) in the garnet core is typical of diffusional homogenization at high temperatures, which results in the obliteration of Fe-Mg growth zoning. Therefore, X_{Fe} of the core is considered to represent the most reasonable parameter for peak-T determination, that should however be considered as a minimum T, because X_{Fe} may have been modified to some extent by diffusion during cooling (see also Indares et al., 2008). Finally, the continuous increase in X_{Fe} toward the rim and in the small garnet relics preserved in the biotite + plagioclase intergrowths (Fig. 2i-l) represents a diffusion-controlled retrograde zoning due to the

exchange of Fe-Mg between garnet rims and biotite during cooling (e.g. Florence and Spear, 1991; Spear, 1991), possibly continuing at sub-*solidus* conditions. From these considerations and following the method proposed by Indares et al. (2008) and Guilmette et al. (pers. com.), the intersection of the X_{Ca} isopleths at the outermost garnet rim and the *solidus* can be inferred to represent the conditions of melt crystallization, whereas the X_{Fe} of the core combined with the X_{Ca} of the garnet rim (see Indares et al., 2008 for a discussion) give a reasonable estimate of the minimum peak-T and P conditions.

Modelling the metamorphic evolution of partially melted rocks is further complicated by possible episodes of melt loss. If some melt loss occurred, then the actually measured bulk rock composition allows the modelling only of the near-to-the-peak and the retrograde evolution, i.e. from the beginning of melt crystallization to the crossing of the *solidus* of the system (White et al., 2004; Indares et al., 2008). We have circumvented this problem by calculating two different pseudosections, representing two defensible end-member cases: (i) a first pseudosection using the measured bulk-rock composition (AR2a, Table 2a), to constrain the P-T evolution from peak temperatures to the complete crystallization of the melt; (ii) a second pseudosection using a bulk composition (AR2b, Table 2a) obtained from one-step melt re-integration following the method of Indares et al. (2008), to evaluate the evolution of the studied sample in the case it started melting at the water saturated *solidus* (i.e. if the rock contained the maximum possible amount of micas).

5.1 Peak and retrograde evolution

Peak and retrograde evolution of sample AR2 were modelled in a first pseudosection calculated in the P-T interval 700-900°C, 5-15 kbar using the measured bulk rock composition AR2a (Table 2a). This pseudosection (Fig. 6a) mainly consists of tri- and quadri-variant fields with minor di-variant fields. Due to the relatively low water content, the *solidus* of the system is located at $T > 800^{\circ}\text{C}$ for $P < 12$ kbar, whereas the *solidus* coincides with the white mica-out reaction at $P > 12$ kbar. At $P < 12$ kbar, the isomodes modelled for all the phases are parallel to the *solidus* (see Fig. A1, available as background dataset): the mineral proportions calculated at the *solidus* (Table 2b) are in good agreement with the observed modal amount of each phase, thus confirming the consistency of the modelling. The peak assemblage melt + garnet + biotite + K-feldspar + plagioclase + kyanite + quartz + rutile is modelled by a tri-variant field (field I in Fig. 6) at $790 < T < 870^{\circ}\text{C}$ and $P > 9$ kbar, at T immediately above the *solidus* and below the biotite-out curve. The maximum amount of melt produced in field I is about 5 vol% at the high-T limit of field I (Fig. 6a).

The intersection between the $X_{Ca}=0.03-0.04$ isopleths at the garnet outer rim (and garnet relics in the biotite + plagioclase intergrowths) and the *solidus* constrains the P-T conditions of melt crystallization at about 805°C , 10 kbar (Fig. 6b). These P-T conditions approximately coincide with the kyanite-sillimanite transition, thus accounting for the local occurrence of sillimanite in the fine-grained biotite-rich domains. The $X_{Fe}=0.78-0.79$ isopleths at the outermost garnet rim are modelled at T immediately below the *solidus* ($730-800^{\circ}\text{C}$; Fig. 6b), thus confirming that the Fe-Mg exchange between garnet rim and biotite may continue, depending upon the cooling rate, at sub-*solidus* conditions.

As previously discussed (cf. section 5), minimum peak-T and P conditions are constrained by the X_{Fe} of garnet core and X_{Ca} of garnet rim at about 820°C , 13 kbar, in the field I. At these P-T conditions the amount of melt produced was very low (ca. 1.5 vol%), significantly lower than the modal amount of fine-grained, biotite-rich domains actually observed in sample AR2 (~ 10 vol%; Fig. 2a) that are interpreted as the sites of melt production and crystallization (see section 4.3).

Therefore, the measured bulk composition cannot represent the composition of the protolith, but should result from some melt extraction during the rock evolution. Further evidence of melt loss is the preservation of the peak assemblage including kyanite and the absence of white mica (see Section 4.3).

5.2 The effects of melt loss

It is impossible to know the amount of melt lost and its composition, thus making it impossible to obtain the exact composition of the sub-*solidus* protolith. However, it has been demonstrated that re-integration of melt into the measured bulk composition is a reasonable method to obtain an approximate protolith composition (e.g. White et al., 2004; Indares et al., 2008). Following the method proposed by Indares et al. (2008), a second pseudosection was calculated using a bulk composition (AR2b, Table 2a) obtained by a one-step melt reintegration into the measured rock composition. The composition of the lost melt was calculated at the intersection of the *solidus* with a presumed prograde P-T path (820°C, 14 kbar). An amount of melt (14 mol%) with that composition, sufficient to bring the *solidus* down temperatures to H₂O saturated conditions, was then added to the bulk composition AR2a. This pseudosection represents the end-member case of a rock containing the maximum possible amount of micas before melting (e.g. Indares et al., 2008), and thus maximizes the extent of the liquid-present fields.

The pseudosection resulting from the melt re-integrated composition AR2b (Fig. 7) differs from the first one in that the *solidus* is considerably shifted down-T (i.e. T<670°C for P<12 kbar, not shown in Fig. 7): therefore there are significant differences between the parts of Fig. 6 at T below the *solidus* (melt-absent fields) and the equivalent parts of Fig. 7 (melt-present fields). The most important differences are that in the melt-reintegrated pseudosection of Fig. 7: (i) the stability of white mica is extended to lower P, and (ii) garnet disappears from the low-T and low-P fields. The variation in garnet stability suggests that, for this approximate protolith composition, garnet grew entirely in the supra-*solidus* domain at T>750°C. As concerning field I, its low-T boundary is slightly shifted down-T, whereas its upper-T boundary remains unchanged. On the contrary, the topologies at the high-T side of the two pseudosections (supra-*solidus* domains of Fig. 6) are very similar (e.g. White and Powell, 2002; Indares et al., 2008), as well as the locations of compositional isopleths within field I (cf. Fig. A2 available as background dataset).

According to the melt-reintegrated pseudosection, at the estimated peak P-T conditions (820°C, 13 kbar) the amount of melt produced was 14-15 vol%. This amount should be considered as a minimum estimate, because the modelled peak-T are minimum-T. The maximum amount of melt produced in field I is around 20 vol%. These amounts of melt are higher than the observed modal percentage of fine-grained biotite-rich domains considered as the sites of melt crystallization (~ 10 vol%, cf. section 4.3), and are also higher than the critical threshold of 7 vol% required for melt to be able to escape from its source (e.g. Rosenberg and Handy, 2005; Brown, 2007). Therefore, the observed modal amount of fine-grained biotite-rich domains (i.e. sites of former melt) is compatible with the production of a 14-20 vol% of melt and its partial extraction during the rock evolution.

5.3 The effects of apatite dissolution and the prograde evolution

The prograde P-T evolution of sample AR2 should be constrained using the prograde growth zoning preserved in the garnet core and Ca-rich annulus. As described in section 4.2 (and Fig. 4), however, the increase in X_{Ca} from the core to the annulus (X_{Ca}=7→15) is sharp and discontinuous. Along any

prograde P-T path that could be envisaged in both pseudosections of Fig. 6 and 7, an increase in X_{Ca} would be more progressive. Therefore other factors, not accounted for in the modelling, should be considered to explain the sharp and discontinuous increase in X_{Ca} from the core to the annulus. Ca zoning in garnet from an anatectic metapelite that resembles the zoning observed in sample AR2 has been interpreted by Indares et al. (2008) as related to apatite dissolution at relatively high pressures. According to this hypothesis, the incorporation of Ca in the melt is not favoured and Ca released from apatite would then be incorporated in garnet. The consequence of this hypothesis is that the growth of the Ca-rich annulus cannot be modelled using bulk compositions AR2a or AR2b, because the increase in X_{Ca} in garnet is controlled by a local change in the effective bulk composition.

A quantitative modelling of the prograde growth of garnet is, therefore, not possible because: (i) the amount of apatite initially present in the protolith, and the amount of apatite dissolved in the melt during anatexis are unknown; (ii) modelling should consider a system with phosphorous as an additional component and apatite as an additional phase, but thermodynamic data for phosphorous-bearing systems are presently lacking. Qualitatively, the increase of CaO available in the system due to apatite dissolution, would cause a shift of the X_{Ca} isopleths of garnet down-P. This, suggests that growth of the Ca-rich annulus may have not necessarily been related to an increase in P, but rather to a local change in the effective bulk composition in the sites of apatite dissolution.

The zoning trends of P, Ti and Y further confirm the reaction history of garnet inferred on the basis of X_{Ca} zoning and P-T pseudosection analysis. The zoning trend of P, combined with that of Ca, may be interpreted as related to the following processes (Fig. 4): (i) apatite was stable during the growth of garnet core, so that Ca and P contents in garnet were at their minimum; (ii) apatite began to dissolve during the growth of the Ca-rich annulus: as a consequence, Ca sharply increases in garnet whereas P, which has a strong affinity for the melt, remained low in garnet; (iii) during the diffusion-controlled retrograde re-equilibration of the garnet outer rim melt began to crystallize, driving a P increase in the remaining melt, which in turn resulted in an increase of P in garnet. As concerning the other trace elements, the Ti increase from garnet core to the Ca-rich annulus may be interpreted as due to prograde growth of garnet via a partial melting reaction involving a Ti-rich phase (biotite and/or phengite), in agreement with the results of pseudosections. The Ti decrease toward the garnet rim may be related to the growth of retrograde biotite through back-reaction with melt. Finally, the Y trend in garnet suggests a prograde dissolution of a Y-phase (Y increased in Grt) followed by the growth of monazite during the formation of the garnet rim and the final melt crystallization (Y decreased in Grt rim) (e.g. Jung and Hellebrand, 2006).

5.4 Conclusions from the modelling

Microstructures, mineral chemistry and zoning, and petrologic modelling allow reconstructing a portion of the P-T evolution of sample AR2. In particular:

- (i) Sample AR2 experienced partial melting in the kyanite stability field, at minimum peak P-T conditions of 820°C, 13 kbar. At these P-T conditions, corresponding to the growth of garnet rim, a maximum of 14-20 vol% of melt was produced;
- (ii) During the following decompression accompanied by a slight cooling, some melt was likely extracted from the source allowing the preservation of the peak assemblage garnet + K-feldspar + kyanite. The remaining ~ 10 vol% of melt progressively crystallized *in situ* leading to the development of the fine-grained biotite + plagioclase domains;

- (iii) Sample AR2 crossed the *solidus* at about 805°C, 10 kbar, i.e. at the kyanite to sillimanite transition;
- (iv) The prograde evolution of sample AR2 cannot be quantitatively modelled on the basis of garnet prograde zoning because the sharp and discontinuous increase in X_{Ca} from the core to the annulus is likely related to a local enrichment in Ca due to apatite dissolution. Modelling of such zoning is therefore hampered by the lack of information on the local effective bulk composition in the sites of apatite dissolution.

From point (iv) it can be more generally concluded that modelling of Ca-poor systems at anatectic conditions appears to be more influenced by apatite dissolution than by episodes of melt loss (see also Indares et al., 2008). Therefore, any attempt to interpret Ca-zoning in garnet from anatectic rocks should carefully consider the possibility that the quantity of CaO available in the system changed during the system evolution in response to apatite dissolution. More specifically, the CaO content in the system is at its minimum as long as apatite is stable, whereas it sharply increases with apatite dissolution. The main consequence of such behaviour is that Ca zoning in garnet is controlled by both the local bulk composition of the system and variations in P-T conditions.

6. Monazite and zircon geochronology

Monazite crystals display a simple planar zoning with parallel broad bands and do not show any evidence of multiple growth domains with cross cutting relationships (Fig. 3c). Monazite includes small crystals of biotite and rounded inclusions rich in Si and Al (SiO_2 80-83 wt%, Al_2O_3 12-13 wt%), which resemble the composition of a granitic melt. The trace element composition of the dated monazite shows little variation. The REE patterns (Fig. 5) are characterised by strong decrease from light- to heavy-REE and a marked negative Eu-anomaly.

U-Pb analysis on twelve grains returned $^{206}Pb/^{238}U$ ages between ~30 and 32 Ma (Table 3). A Concordia age of 31.0 ± 0.4 Ma (Fig. 8) is defined by eleven analyses with the exclusion of the youngest analysis, which has a higher Th content. The Th-Pb system returns similar ages with an average of 30.6 ± 0.6 (MSWD 1.3, N=11). The agreement between the two systems excludes the presence of significant excess ^{206}Pb from the decay of ^{230}Th .

Zircons from sample AR2 preserve a more complex internal structure than the monazite (Fig. 3d-f). The crystals are volumetrically dominated by oscillatory zoned cores, which have a variety of zoning patterns, as commonly observed in metasediments. The cores are surrounded by thin CL-dark rims that only occasionally are large enough ($>20 \mu m$) for SHRIMP analysis. The $^{206}Pb/^{238}U$ age of the 22 zircon cores dated scatter greatly between ~1590 and 425 Ma with a number of discordant analyses (Table 4). The youngest group of concordant analyses is at ~445 Ma (444.5 ± 4.4 Ma, 95% confidence level, MSWD = 0.53, N=4). These domains are rich in U (up to 450-2270 ppm) and have a variable Th/U ratio (0.01-0.14).

The zircon rims have low Th/U (0.01-0.02) and are extremely rich in U with concentrations up to 8900 ppm. Such high concentrations are known to produce a matrix effect (Butera et al., 2004), which has been documented to be significant above ~2500 ppm of U and leads to ages ~3% older for each 1000 ppm of U (Butera et al. 2004, Hermann et al. 2006 and Rubatto unpublished data). When such matrix correction is applied to analyses with more than 2500 ppm of U, the clustering of the ages improve but remains poor around 27-29 Ma with scatter above analytical uncertainty. At this level of uncertainty, and no apparent CL or compositional difference between the zircon rims, it is impossible to split the population and thus the zircon rim formation age is constrained to a period

between ~27-29 Ma. One single analysis remains significantly younger (apparent $^{206}\text{Pb}/^{238}\text{U}$ age 20.4 ± 0.3 Ma).

7. Discussion

7.1 Kyanite-bearing migmatites in the MCTZ

This study documents the presence, at the highest structural levels of the MCTZ, of partially melted rocks formed in the kyanite stability field. Partial melting within the MCTZ has been previously recognised in Eastern Nepal by Goscombe et al. (2006) (Arun-Makalu and Tamor-Yangma transects) and by Groppo et al. (2009) (Milke Danda transect), with the latter authors reporting a P-T evolution for the anatectic rocks. The P-T path of sample AR2 is indeed similar to that of migmatites from the Milke Danda transect (sample 38 in Groppo et al., 2009), only shifted at slightly higher pressures and temperatures. Dehydration partial melting occurred in the kyanite stability field, implying that melt was present at pressures > 9-10 kbar. After reaching peak metamorphic conditions at $T \geq 820^\circ\text{C}$, 13 kbar, sample AR2 experienced decompression accompanied by cooling down to ca. 805°C , 10 kbar (Fig. 9), which caused *in situ* melt crystallization (i.e. in the fine-grained biotite-rich domains), the development of back-reaction microstructures (i.e. the biotite + plagioclase intergrowths, Fig. 2i-l) and the late growth of prismatic sillimanite (Fig. 3a).

These petrologic results demonstrate that in the upper MCTZ, at least in the eastern Himalaya, crustal anatexis was earlier than, and not a consequence of, decompression linked to exhumation along the MCT. On this basis, the MCTZ anatectic rocks may be distinguished from anatectic rocks occurring in the structurally higher HHC. In the HHC, in fact, crustal anatexis is generally interpreted as a consequence of nearly isothermal decompression from the kyanite to the sillimanite field (e.g. Pognante and Benna, 1993; Harris et al., 2004; Viskupic et al., 2005).

7.2 Early Oligocene crustal anatexis

AR2 monazite yielded a straightforward age at 31.0 ± 0.4 Ma. Textural relationships indicate that monazite is present as inclusions in the garnet rim and in the matrix. Additionally, the presence of likely melt inclusions suggests that monazite formed in the melt field when the garnet rim was growing (i.e. at peak P-T conditions, see section 5.1 and Fig. 9). Additional information about the relative timing of monazite and garnet formation can be obtained from monazite-garnet trace element partitioning. A number of works have established that the equilibrium partitioning between monazite and garnet systematically decreases from Sm to Lu from ~18000 to 2-3 (Rubatto, 2002; Buick et al. 2006; Rubatto et al. 2006). For the studied sample the trace element partitioning is calculated between average monazite and representative analyses from the three garnet zones (core, Ca-rich annulus, and rims) (Fig. 5c). Of the calculated partitioning, the range of partitioning with the garnet core and the Ca-rich annulus is inconsistent with published equilibrium data, whereas the partitioning between monazite and garnet rim is overlapping with published data, particularly with the data of Rubatto et al. (2006). Therefore, microstructures, inclusions and trace element partitioning allow relating the age of monazite to that of melting and garnet rim growth.

The Himalayan zircon rims are euhedral in shape, they texturally grow on partly resorbed cores (Fig. 3d-f) and contain high amounts of U. These are features common to anatectic zircon overgrowths (e.g. Rubatto et al., 2001, 2009) and together with the low reactivity of zircon in subsolidus conditions (Rubatto et al. 2001), suggest zircon dissolution and re-precipitation during melting. The possible implication is that melt persisted over a few million years from the formation

of monazite at 31.0 ± 0.4 Ma to the crystallisation of zircon rims at 29-27 Ma (Fig. 9). Such a scenario would also explain the additional scatter in the zircon ages.

The monazite and zircon ages obtained for the studied sample thus provide clear evidence of an early-Oligocene anatexis in the kyanite stability field, affecting the upper portion of the MCTZ. To our knowledge this is the first report of such an old age at this structural level. Kohn et al. (2001) and Daniel et al. (2003) report maximum monazite ages of 18-22 Ma for the upper MCTZ in the Darondi region (central Nepal) and Bhutan, respectively, but no anatectic rocks have been dated in both cases.

Acknowledgements

Fieldwork was carried out thanks to contributions from the Italian National Research Council (B.L. and F.R.) and from PRIN Cofin 2006 (C.G.). Laboratory work was supported by PRIN Cofin 2006 (national coordinator E. Garzanti). The Electron Microscopy Unit at the Australian National University is thanked for access to the SEM facilities. We gratefully acknowledge M. Searle for his helpful review, though the authors' views of regional geology may remain different, and A. Indares for her in-depth and constructive comments and very useful suggestions about the thermodynamic modelling of high-P anatectic samples. D.R. acknowledges the support of the Australian Research Council through a QEII Fellowship and Discovery Project DP0556700.

References

- Álvarez-Valero, A.M., Kriegsman, L.M., 2010. Melt-producing versus melt-consuming reactions in pelitic xenoliths and migmatites. *Lithos*, in press (doi: 10.1016/j.lithos.2009.09.001)
- Andrews, E., 1985. Stratigraphy of the Sabhaya Khola region, Sankhuwa Sabha District, eastern Nepal. *Journal of Nepal Geological Society* 2, 12–35.
- Black, L.P., Kamo, S.L., Allen, C.M., Aleinikoff, J.M., Davis, D.W., Korsch, R.J., Foudoulis, C., 2003. TEMORA 1: a new zircon standard for Phanerozoic U-Pb geochronology. *Chemical Geology* 200, 155–170.
- Bordet, P., 1961. Recherches géologiques dans l'Himalaya du Népal, région du Makalu. Editions du Centre National de la Recherche Scientifique, Paris, 275 pp.
- Bordet, P., 1977. Géologie de la dalle du Tibet (Himalaya central). Mémoires hors série de la Société Géologique de France 8, 235–250.
- Brown, M., 2007. Crustal melting and melt extraction, ascent and emplacement in orogens : mechanism and consequences. *Journal of Geological Society of London* 164, 709–730.
- Brunel, M., Kienast, J.R., 1986. Etude pétro-structurale des chevauchements ductiles himalayens sur la transversale de l'Everest-Makalu (Népal oriental). *Canadian Journal of Earth Sciences* 23, 1117–1137.
- Buick, I.S., Hermann, J., Williams, I.S., Gibson, R., Rubatto, D., 2006. A SHRIMP U-Pb and LA-ICP-MS trace element study of the petrogenesis of garnet-cordierite-orthoamphibole gneisses from the Central Zone of the Limpopo Belt, South Africa. *Lithos* 88, 150–172.
- Burchfiel, B.C., Chen, Z., Hodges, K.V. et al., 1992. The South Tibetan Detachment System, Himalayan Orogen: Extension Contemporaneous with and Parallel to Shortening in a Collisional Mountain Belt. Special Paper 269. Geological Society of America, Boulder, CO, 41 pp.
- Butera, K.M., Williams, I.S., Blevin, P.L., Simpson, C.J., 2004. Zircon U-Pb dating of Early Palaeozoic monzonitic intrusives from the Goonumbla area, New South Wales. *Australian Journal of Earth Sciences* 48, 457–464.
- Carosi, R., Lombardo, B., Molli, G., Musumeci, G., Pertusati, P.C., 1998. The South Tibetan detachment system in the Rongbuk Valley, Everest region. Deformation features and geological implications. *Journal of Asian Earth Sciences* 16, 299–311.
- Catlos, E.J., Dubey, C.S., Harrison, T.M., Edwards, M.A., 2004. Late Miocene movement within the Himalayan Main Central Thrust shear zone, Sikkim, north-east India. *Journal of Metamorphic Geology* 22, 207–226.
- Cenki, B., Kriegsman, L.M., Braun, I., 2002. Melt-producing and melt-consuming reactions in the Achankovil cordierite gneisses, South India. *Journal of Metamorphic Geology* 20, 543–561.
- Coleman, M.E., Hodges, K.V., 1998. Contrasting Oligocene and Miocene thermal histories from the hanging wall of the South Tibetan detachment in the central Himalaya from $^{40}\text{Ar}/^{39}\text{Ar}$ thermochronology, Marsyandi valley, central Nepal. *Tectonics* 17, 726–740.
- Coleman, M.E., 1998. U-Pb constraints on Oligocene–Miocene deformation and anatexis within the central Himalaya, Marsyandi Valley, Nepal. *American Journal of Science* 298, 553–571.
- Connolly, J.A.D., 1990. Multivariable phase diagrams: an algorithm based on generalized thermodynamics. *American Journal of Science* 290, 666–718.
- Connolly, J.A.D., 2009. The geodynamic equation of state: what and how. *Geochemistry, Geophysics, Geosystems* 10, Q10014.
- Cottle, J.M., Searle, M.P., Horstwood, M.S.A., Waters, D.J., 2009. Midcrustal metamorphism, melting, and deformation in the Mount Everest region of Southern Tibet revealed by U(-Th)-Pb geochronology. *The Journal of Geology* 117, 643–664.
- Daniel, C.G., Hollister, L.S., Parrish, R.R., Grujic, D., 2003. Exhumation of the Main Central Thrust from lower crustal depths, Eastern Bhutan Himalaya. *Journal of Metamorphic Geology* 21, 317–334.

- Dasgupta, S., Chakraborty, S., Neogi, S., 2009. Petrology of an inverted Barrovian sequence of metapelites in Sikkim Himalaya, India: constraints on the tectonics of inversion. *American Journal of Science* 309, 43–84.
- Dasgupta, S., Ganguly, J., Neogi, S., 2004. Inverted metamorphic sequence in the Sikkim Himalayas: crystallization history, P–T gradient and implications. *Journal of Metamorphic Geology* 22, 395–412.
- Dietrich, V., Gansser, A., 1981. The leucogranites of the Bhutan Himalaya (crustal anatexis versus mantle melting). *Schweizerische Mineralogische und Petrographische Mitteilungen* 61, 177–202.
- Edwards, M.A., Harrison, T.M., 1997. When did the roof collapse? Late Miocene north–south extension in the high Himalaya revealed by Th–Pb monazite dating of the Khula Kangri granite. *Geology* 25, 543–546.
- Eggins, S.M., Rudnick, R.L., McDonough, W.F., 1998. The composition of peridotites and their minerals: a laser ablation ICP-MS study. *Earth and Planetary Science Letters* 154, 53–71.
- Ferrara, G., Lombardo, B., Tonarini, S., 1983. Rb/Sr geochronology of granite and gneisses from the Mount Everest Region, Nepal Himalaya. *Geologische Rundschau* 72, 119–136.
- Florence, F.P., Spear, F.S., 1991. Effects of diffusional modification of garnet growth zoning on P–T path calculations. *Contributions to Mineralogy and Petrology* 107, 487–500.
- Fraser, G., Worley B., Sandiford, M., 2000. High-precision geothermobarometry across the High Himalayan metamorphic sequence, Langtang Valley, Nepal. *Journal of Metamorphic Geology* 18, 665–681.
- Godin, L., Parrish, R.R., Brown, R.L., Hodges, K.V., 2001. Crustal thickening leading to exhumation of the Himalayan metamorphic core of central Nepal: Insights from U–Pb geochronology and $^{40}\text{Ar}/^{39}\text{Ar}$ thermochronology. *Tectonics* 20, 729–747.
- Goscombe, B., Gray, D., Hand, M., 2006. Crustal architecture of the Himalayan metamorphic front in eastern Nepal. *Gondwana Research* 10, 232–255.
- Goscombe, B., Hand, M., 2000. Contrasting P–T paths in the Eastern Himalaya, Nepal: inverted isograds in a paired metamorphic mountain belt. *Journal of Petrology* 41, 1673–1719.
- Groppo, C., Rolfo, F., Lombardo, B., 2009. P–T evolution across the Main Central Thrust Zone (Eastern Nepal): hidden discontinuities revealed by petrology. *Journal of Petrology* 50, 1149–1180.
- Grujic, D., Casey, M., Davidson, C., Hollister, L.S., Kundig, R., Pavlis, T., Schmid, S., 1996. Ductile extrusion of the Higher Himalayan crystalline in Bhutan: evidence from quartz microfabrics. *Tectonophysics* 260, 21–43.
- Guillot, S., 1999. An overview of the metamorphic evolution in central Nepal. *Journal of Asian Earth Sciences* 17, 713–725.
- Hagen, T., 1969. Report on the geological survey of Nepal, v. 1, Preliminary reconnaissance. *Memoires de la Soci  t   Helv  tique des Sciences Naturelles* 86, 185 p.
- Halpin, J.A., Clarke, C.L., White, R.W., Kelsey, D.E., 2007. Contrasting P–T–t paths for Neoproterozoic metamorphism in MacRobertson and Kemp lands, east Antarctica. *Journal of Metamorphic Geology* 25, 683–701.
- Harris, N.B.W., Caddick, M., Kosler, J., Goswami, S., Vance, D., Tindle, A.G., 2004. The pressure–temperature–time path of migmatites from Sikkim Himalaya. *Journal of Metamorphic Geology* 22, 249–264.
- Hermann, J., Rubatto, D., 2003. Relating zircon and monazite domains to garnet growth zones: age and duration of granulite facies metamorphism in the Val Malenco lower crust. *Journal of Metamorphic Geology* 21, 833–852.
- Hermann, J., Rubatto, D., Trommsdorff, V., 2006. Sub-solidus Oligocene zircon formation in garnet peridotite during fast decompression and fluid infiltration (Duria, Central Alps). *Mineralogy and Petrology* 88, 181–206.
- Hodges, K.V., Bowring, S., Davidek, K., Hawkins, D., Krol, M., 1998. Evidence for rapid displacement on Himalayan normal faults and the importance of tectonic denudation in the evolution of mountain ranges. *Geology* 26, 483–486.

- Hodges, K.V., Hubbard, M.S., Silverberg, D.S., 1988. Metamorphic constraints on the thermal evolution of the central Himalayan Orogen. *Philosophical Transactions of the Royal Society of London A* 326, 257–280.
- Hodges, K.V., Parrish, R.R., Searle, M.P., 1996. Tectonic evolution of the central Annapurna Range, Nepalese Himalayas. *Tectonics* 15, 1264–1291.
- Holland, T.J.B., Powell, R., 1998. An internally consistent thermodynamic data set for phases of petrologic interest. *Journal of Metamorphic Geology* 16, 309–343.
- Holland, T.J.B., Powell, R., 2001. Calculation of phase relations involving haplogranitic melts using an internally consistent thermodynamic dataset. *Journal of Petrology* 42, 673–683.
- Holness, M.B., Clemens, J.D., 1999. Partial melting of the Appin Quartzite driven by fracture controlled H₂O infiltration in the aureole of the Ballachulish Igneous Complex, Scottish Highlands. *Contributions to Mineralogy and Petrology* 136, 154–168.
- Holness, M.B., Sawyer, E.W., 2008. On the pseudomorphing of melt-filled pores during the crystallization of migmatites. *Journal of Petrology* 49, 1343–1363.
- Hubbard, M.S., 1989. Thermobarometric constraints on the thermal history of the Main Central Thrust Zone and Tibetan Slab, eastern Nepal, Himalaya. *Journal of Metamorphic Geology* 7, 19–30.
- Indares, A., White, R.W., Powell, R., 2008. Phase equilibria modelling of kyanite-bearing anatectic paragneiss from the central Grenville Province. *Journal of Metamorphic Geology* 26, 815–836.
- Inger, S., Harris, N.B.W., 1992. Tectonothermal evolution of the High Himalayan Crystalline Sequence, Langtang Valley, northern Nepal. *Journal of Metamorphic Geology* 10, 439–452.
- Jessup, M.J., Newell, D.L., Cottle, J.M., Berger, A.L., Spotila, J.A., 2008. Orogen-parallel extension and exhumation enhanced by denudation in the trans-Himalayan Arun River gorge, Ama Drime Massif, Tibet-Nepal. *Geology* 36, 587–590.
- Jung, S., Hellebrand, E., 2006. Trace element fractionation during high-grade metamorphism and crustal melting – constraints from ion microprobe data of metapelitic, migmatitic and igneous garnets and implications for Sm-Nd garnet chronology. *Lithos* 87, 193–213.
- Kohn, M.J., Catlos, E.J., Ryerson, F.J., Harrison, T.M., 2001. Pressure-temperature-time path discontinuity in the Main Central Thrust Zone, central Nepal. *Geology* 29, 571–574.
- Kohn, M.J., Spear, F.S., Valley, J.W., 1997. Dehydration melting and fluid recycling during metamorphism: Rangeley Formation, New Hampshire, USA. *Journal of Petrology* 38, 1255–1277.
- Kohn, M.J., Wieland, M.S., Parkinson, C.D., Upreti, B.N., 2005. Five generations of monazite in Langtang gneisses: implications for chronology of the Himalayan metamorphic core. *Journal of Metamorphic Geology* 23, 399–406.
- Le Fort, P., 1975. Himalaya: the collided range. Present knowledge of the continental arc. *American Journal of Science* 275A, 1–44.
- Lombardo, B., Pertusati, P., Borghi, A., 1993. Geology and tectono-magmatic evolution of the eastern Himalaya along the Chomolungma-Makalu transect. In: Treloar, P. J., Searle, M.P. (eds.) *Himalayan Tectonics*. Geological Society of London, Special Publication 74, 341–355.
- Lombardo, B., Borghi, A., Pertusati, P., 1998. Metamorphism in the Tibetan slab of the Arun valley and Everest massif, Nepal and southern Tibet. *Geological Bulletin, University of Peshawar, Special Issue* 31, 118–119.
- Ludwig, K.R., 2003. Isoplot/Ex version 3.0. A geochronological toolkit for Microsoft Excel. 1a, Berkeley Geochronological Centre Special Publication, Berkeley.
- Macfarlane, A.M., 1995. An evaluation of the inverted metamorphic gradient at Langtang National Park, Central Nepal, Himalaya. *Journal of Metamorphic Geology* 13, 595–612.
- Meier, K., Hiltner, E., 1993. Deformation and metamorphism within the Main Central Thrust zone, Arun tectonic Window, eastern Nepal. In: Treloar, P.J., Searle, M.P. (eds.) *Himalayan Tectonics*. Geological Society of London, Special Publication 74, 511–523.

- Newton, R.C., Charlu, T.V., Kleppa, O.J., 1980. Thermochemistry of the high structural state plagioclases. *Geochimica et Cosmochimica Acta* 44, 933–941.
- Paces, J.B., Miller, J.D., 1993. U-Pb ages of the Duluth complex and related mafic intrusions, northeastern Minnesota: geochronologic insights into physical petrogenetic, paleomagnetic and tectonomagmatic processes associated with the 1.1 Ga mid-continent rift system. *Journal of Geophysical Research* 98, 13,997–14,013.
- Pearce, N.J.G., Perkins, W.T., Westgate, J.A., Gorton, M.P., Jackson, S.E., Neal, C.R., Chenery, S.P., 1997. A compilation of new and published major and trace element data for NIST SRM 610 and NIST SRM 612 glass reference materials. *Geostandards Newsletter - the Journal of Geostandards and Geoanalysis* 21, 115–144.
- Pêcher, A., 1989. The metamorphism in the Central Himalaya. *Journal of Metamorphic Geology* 7, 31–41.
- Pognante, U., Benna, P., 1993. Metamorphic zonation, migmatization, and leucogranites along the Everest transect (Eastern Nepal and Tibet): record of an exhumation history. In: Treloar, P.J., Searle M.P. (eds.) *Himalayan Tectonics*. Geological Society of London, Special Publication 74, 323–340.
- Pouchou, J.L., Pichoir, F., 1988. Determination of mass absorption coefficients for soft X-Rays by use of the electron microprobe. *Microbeam Analysis*, San Francisco Press, 319–324.
- Powell, R., Holland, T., 1999. Relating formulations of the thermodynamics of mineral solid solutions: Activity modeling of pyroxenes, amphiboles, and micas. *American Mineralogist* 84, 1–14.
- Powell, R., Holland, T.J.B., 2008. On thermobarometry. *Journal of Metamorphic Geology* 26, 155–179.
- Rosenberg, C.L., Handy, M.R., 2005. Experimental deformation of partially melted granite revisited: implications for the continental crust. *Journal of Metamorphic Geology* 23, 19–28.
- Rubatto, D., 2002. Zircon trace element geochemistry: distribution coefficients and the link between U-Pb ages and metamorphism. *Chemical Geology* 184, 123–138.
- Rubatto, D., Hermann, J., Berger, A., Engi, M., 2009. Protracted fluid-induced melting during Barrovian metamorphism in the Central Alps. *Contributions to Mineralogy and Petrology*, 158, 703–722.
- Rubatto, D., Hermann, J., Buick, I.S., 2006. Temperature and bulk composition control on the growth of monazite and zircon during low-pressure anatexis (Mount Stafford, central Australia). *Journal of Petrology* 47, 1973–1996.
- Rubatto, D., Williams, I.S., Buick, I.S., 2001. Zircon and monazite response to prograde metamorphism in the Reynolds Range, central Australia. *Contributions to Mineralogy and Petrology* 140, 458–468.
- Searle, M.P., 1999. Extensional and compressional faults in the Everest-Lhotse massif, Khumbu Himalaya, Nepal. *Journal of the Geological Society, London*, 156, 227–240.
- Searle, M.P., Godin, L., 2003. The South Tibetan Detachment and the Manaslu Leucogranite: a structural reinterpretation and restoration of the Annapurna-Manaslu Himalaya, Nepal. *Journal of Geology* 111, 505–523.
- Searle, M.P., Law, R.D., Godin, L., Larson, K.P., Streule, M.J., Cottle, J.M., Jessup, M.J., 2008. Defining the Himalayan Main Central Thrust in Nepal. *Journal of the Geological Society, London* 165, 523–534.
- Searle, M.P., Parrish, R.R., Hodges, K.V., Hurford, A., Ayres, M.W., Whitehouse, M.J., 1997. Shisha Pangma leucogranite, south Tibetan Himalaya: Field relations, geochemistry, age, origin, and emplacement. *Journal of Geology* 105, 295–317.
- Searle, M.P., Simpson, R.L., Law, R.D., Parrish, R.R., Waters, D.J., 2003. The structural geometry, metamorphic and magmatic evolution of the Everest massif, High Himalaya of Nepal-South Tibet. *Journal of the Geological Society* 160, 345–366.
- Shresta, S.B., Shresta, J.N., Sharma, S.R., 1984. Geological Map of Eastern Nepal, 1:250,000. Lainchour, Kathmandu, Ministry of Industry, Department of Mines and Geology.
- Simpson, R.L., Parrish, R.R., Searle, M.P., Waters, D.J., 2000. Two episodes of monazite crystallization during metamorphism and crustal melting in the Everest region of the Nepalese Himalaya. *Geology* 28, 403–406.

- Spear, F.S., 1991. On the interpretation of peak metamorphic temperatures in light of garnet diffusion during cooling. *Journal of Metamorphic Geology* 9, 379–388.
- Spear, F.S., Hickmott, D.D., Selverstone, J., 1990. Metamorphic consequences of thrust emplacement, Fall Mountain, New Hampshire. *Geological Society of America Bulletin* 102, 1344–1360.
- Spear, F.S., Kohn, M.J., Cheney, J.T., 1999. P-T paths from anatectic pelites. *Contributions to Mineralogy and Petrology* 134, 17–32.
- Stacey, J.S., Kramers, J.D., 1975. Approximation of terrestrial lead evolution by a two-stage model. *Earth and Planetary Science Letters* 26, 207–221.
- Tonarini, S., Lombardo, B., Ferrara, G., Marcassa, P., 1994. Partial melting in the Namche Migmatite of Khumbu Himal (Nepal Himalaya). *Mineralogical and Petrological Acta* 37 (Fornaseri volume), 277–294.
- Vannay, J.C., Hodges, K.V., 1996. Tectonometamorphic evolution of the Himalayan metamorphic core between the Annapurna and Dhaulagiri, central Nepal. *Journal of Metamorphic Geology* 14, 635–656.
- Viskupic, K., Hodges, K.V., 2001. Monazite–xenotime thermochronometry: methodology and an example from the Nepalese Himalaya. *Contributions to Mineralogy and Petrology* 141, 233–247.
- Viskupic, K., Hodges, K.V., Bowring, S.A., 2005. Timescales of melt generation and the thermal evolution of the Himalayan metamorphic core, Everest region, eastern Nepal. *Contributions to Mineralogy and Petrology* 149, 1–21.
- Visonà, D., Lombardo, B., 2002. Two mica- and tormaline leucogranites from the Everest-Makalu region (Nepal-Tibet): Himalayan leucogranite genesis by isobaric heating? *Lithos* 62, 125–150.
- Waldbaum, D.R., Thompson, J.B., 1969. Mixing properties of sanidine crystalline solutions II. Calculations based on volume data. *American Mineralogist* 53, 2000–2017.
- Waters, D.J., 2001. The significance of prograde and retrograde quartz-bearing intergrowth microstructures in partially melted granulite-facies rocks. *Lithos* 56, 97–110.
- White, R.W., Powell, R., Halpin, A., 2004. Spatially-focussed melt formation in aluminous metapelites from Broken Hill, Australia. *Journal of Metamorphic Geology* 22, 825–845.
- White, R.W., Powell, R., Holland, T.J.B., 2001. Calculation of partial melting equilibria in the system $\text{Na}_2\text{O}-\text{CaO}-\text{K}_2\text{O}-\text{FeO}-\text{MgO}-\text{Al}_2\text{O}_3-\text{SiO}_2-\text{H}_2\text{O}$ (NCKFMASH). *Journal of Metamorphic Geology* 19, 139–153.
- White, R.W., Powell, R., Holland, T.J.B., 2007. Progress relating to calculation of partial melting equilibria for metapelites. *Journal of Metamorphic Geology* 25, 511–527.
- White, R.W., Powell, R., Holland, T.J.B., Worley, B.A., 2000. The effect of TiO_2 and Fe_2O_3 on metapelitic assemblages at greenschist and amphibolite facies conditions: mineral equilibria calculations in the system $\text{K}_2\text{O}-\text{FeO}-\text{MgO}-\text{Al}_2\text{O}_3-\text{SiO}_2-\text{H}_2\text{O}-\text{TiO}_2-\text{Fe}_2\text{O}_3$. *Journal of Metamorphic Geology* 18, 497–511.
- White, R.W., Powell, R., 2002. Melt loss and the preservation of granulite facies mineral assemblages. *Journal of Metamorphic Geology* 20, 621–632.
- Williams, I.S., 1998. U-Th-Pb geochronology by ion microprobe. In: McKibben, M.A., Shanks, W.C., Ridley, W.I. (Eds.), *Application of microanalytical techniques to understanding mineralizing processes. Reviews in Economic Geology, Society of Economic Geologists*, pp. 1–35.

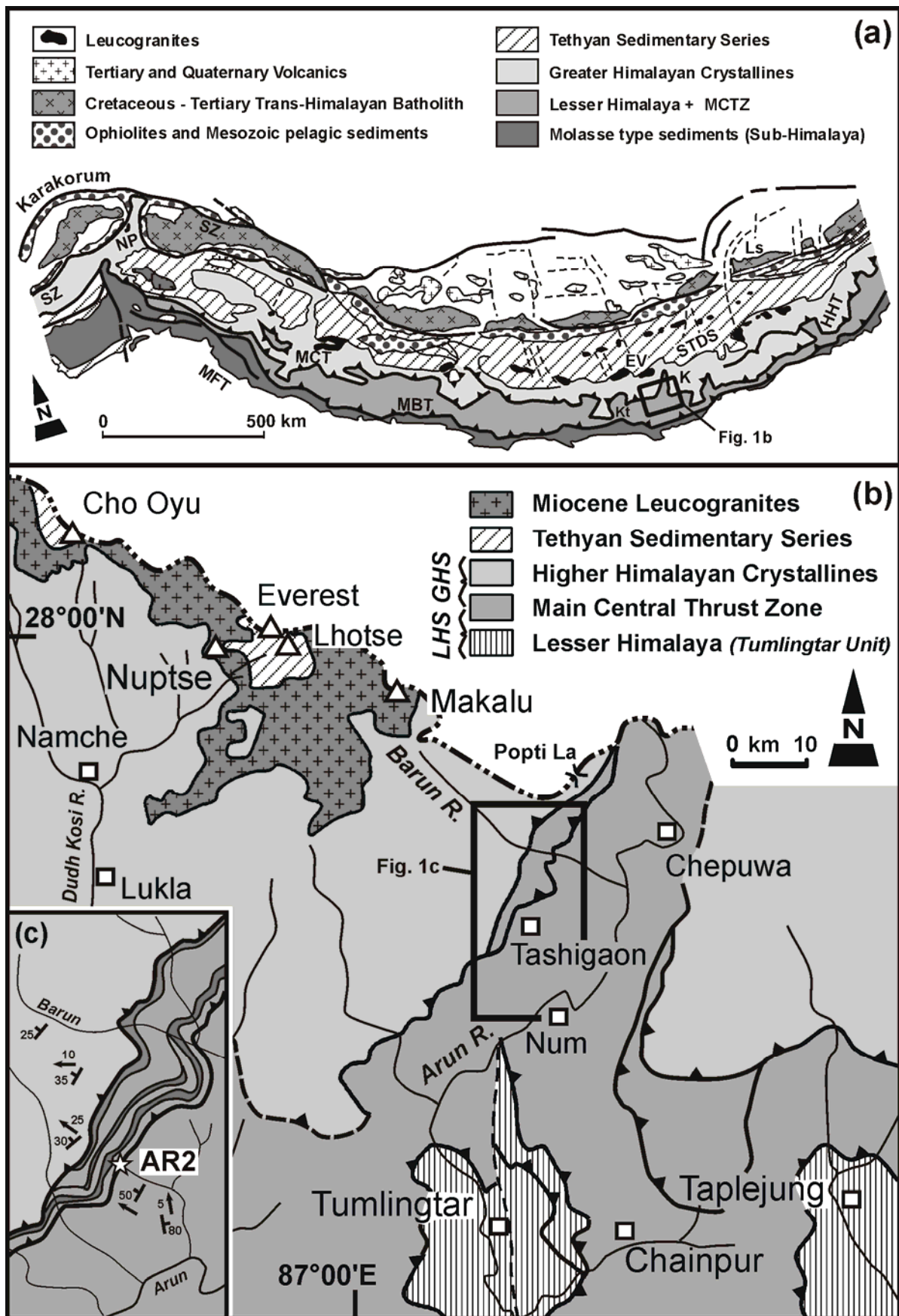


Fig. 1 – (a) Geological sketch map of the Himalaya and southern Tibetan Plateau (modified after Groppo et al., 2009 and based on Dietrich and Gansser, 1981). SZ = Indus/Yarlung Tsangpo Suture Zone; MFT = Main Frontal Thrust; MBT = Main Boundary Thrust; MCT = Main Central Thrust; HHT = High Himal Thrust;

STDS = South Tibetan Detachment System; NP = Nanga Parbat; EV = Everest; K = Kangchendzonga; Kt = Kathmandu; Ls = Lhasa. (b) Geological sketch map of eastern Nepal from Cho Oyu to Taplejung across the middle Arun drainage and the Arun Tectonic Window, after Groppo et al. (2009). The north limit of the map (double dashed line) is the approximate political boundary between Nepal to the south, and China (Tibet) to the north. The Lesser Himalayan Sequence (LHS) and the Greater Himalayan Sequence (GHS) are *sensu* Goscombe et al. (2006). (c) Enlargement across the Main Central Thrust Zone between the Arun and Barun rivers, showing the location of the studied sample AR2. Tectonic contacts define a number of thrust sheets within the upper sector of the Main Central Thrust Zone. Geology based on Bordet (1961), Lombardo et al. (1993), Goscombe and Hand (2000) and authors' observations.

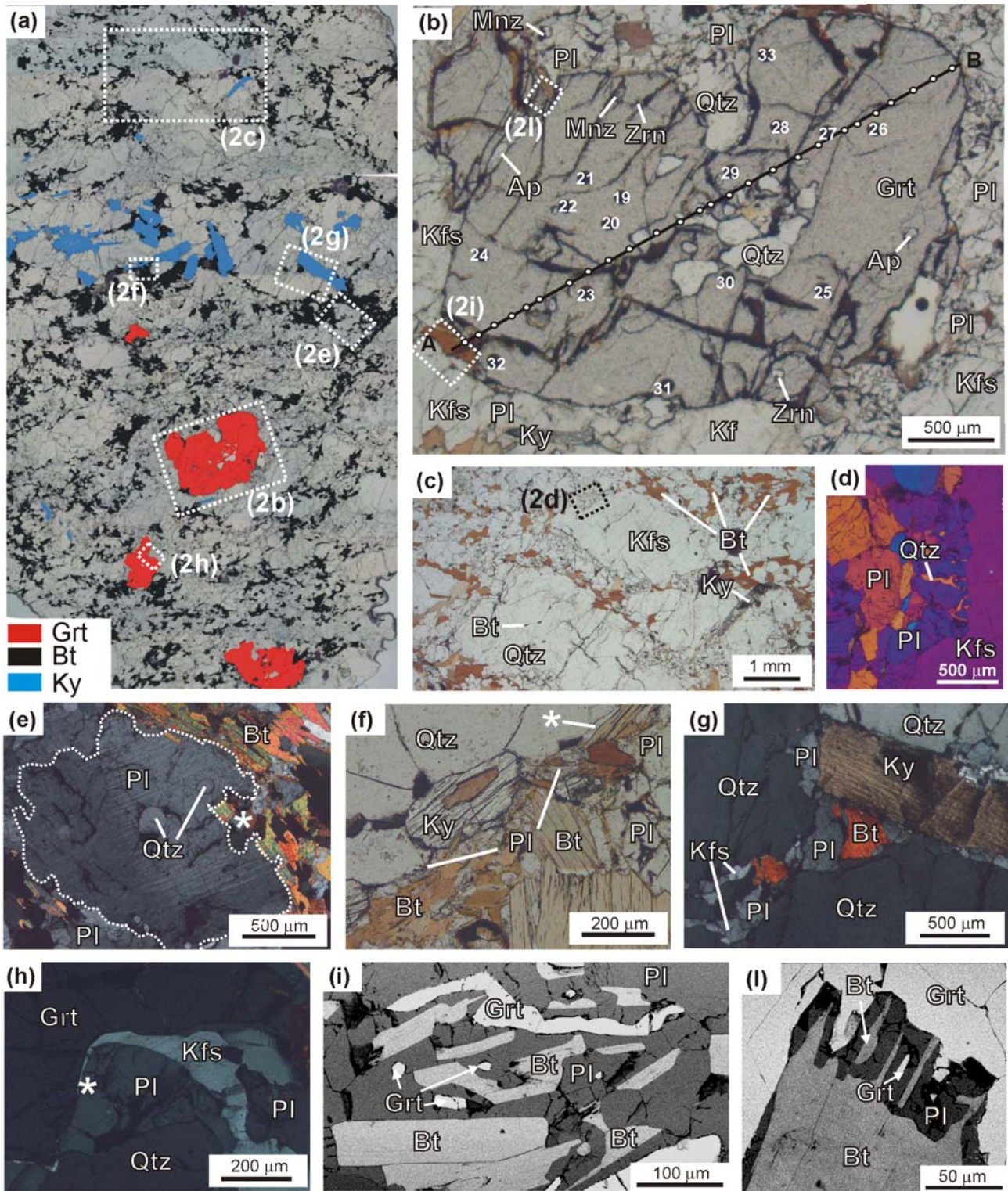


Fig. 2 – (a) Microphoto of the whole thin section showing the microstructure of sample AR2. The microstructure is characterized by fine-grained biotite-rich domains wrapping around coarse-grained elongated kyanite-bearing quartzo-feldspathic domains and garnet porphyroblasts. Biotite, garnet and kyanite are coloured in black, red and blue respectively, and their modal percentage has been estimated by image analysis. (b) Detail of a garnet porphyroblast, with lobate quartz inclusions in the core. Note monazite and zircon inclusions in garnet rim. Line A-B locates the compositional profile of Fig. 4. Numbers refer to laser ablation spots reported in Fig. 4. Plane Polarized light (PPL). (c) Detail of the coarse-grained, residual K-feldspar and quartz wrapped around by the fine-grained biotite + plagioclase domains interpreted as the sites

of melt crystallization (PPL). (d) Detail of a myrmekite partially corroding a K-feldspar porphyroblast. Crossed Polarized light (XPL) with first-order red plate. (e) Plagioclase porphyroblast with quartz inclusions, partially corroded by the fine-grained biotite + plagioclase domain (see the asterisk) (XPL). (f) Detail of a kyanite crystal located at the contact between a fine-grained biotite-rich layer (bottom right) and a coarse-grained quartz-feldspathic domain (top left). Biotite inclusions in kyanite likely escaped anatexis. The asterisk indicates a pseudomorph of liquid-filled pore consisting of an optical continuous crystal of plagioclase (PPL). (g) Detail of kyanite-quartz interfaces in a coarse-grained domain. Kyanite appears in equilibrium with quartz (upper right) except where in communication with the fine-grained biotite-rich domains, where it is surrounded by plagioclase + biotite (XPL). (h) Detail of a pseudomorph of liquid-filled pores consisting of an optical continuous crystal of K-feldspar with low dihedral angles (see asterisk) against garnet (XPL). (i, l) Detail of the biotite + plagioclase intergrowths representing the final stages of back reactions involving melt crystallization (Waters, 2001). Note the small garnet relics in both images (Back Scattered Electron image, BSE).

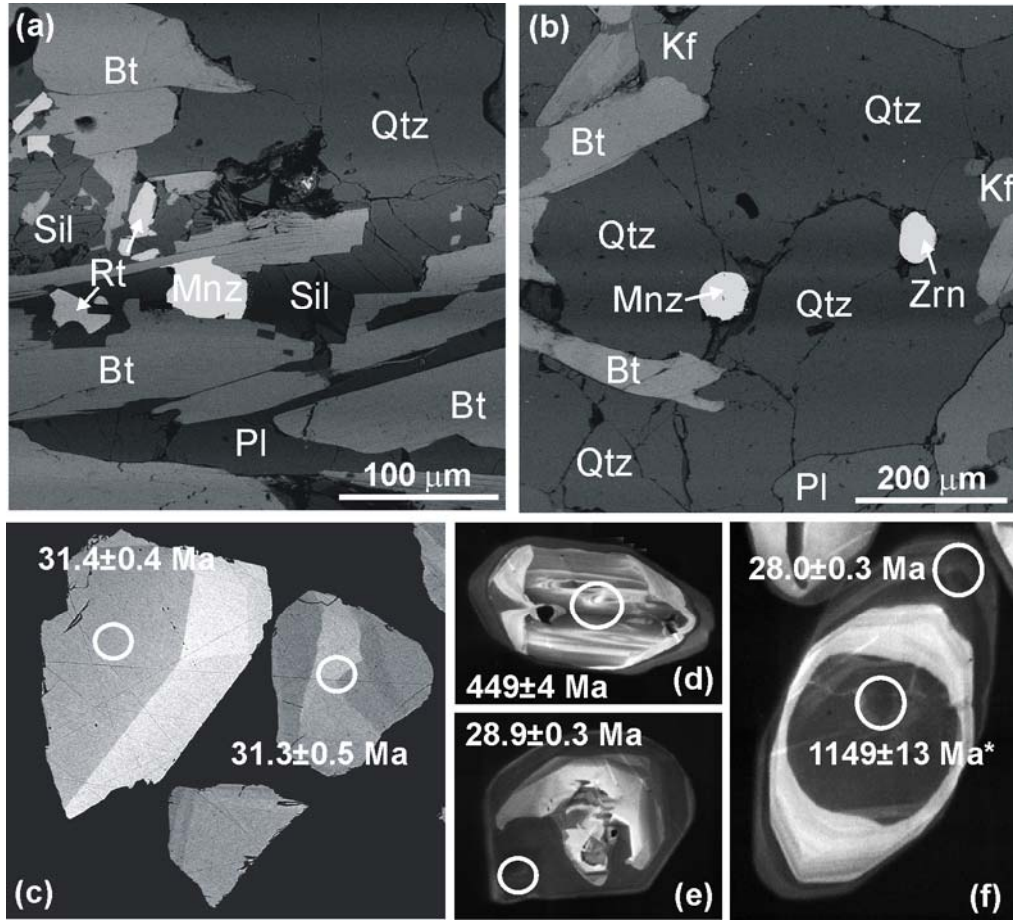


Fig. 3 – (a, b) BSE images showing the microstructural position of monazite and zircon in the fine-grained biotite-rich domains. Note in (a) sillimanite overgrowing biotite flakes. (c) BSE images of separated monazite grains showing a simple planar zoning. (d, e, f) Cathodoluminescence (CL) images of zircon crystals with oscillatory zoned cores overgrown by a CL-dark unzoned rim. In (c-f) numbers refer to $^{206}\text{Pb}/^{238}\text{U}$ ages in $\text{Ma} \pm 1$ sigma or $^{207}\text{Pb}/^{206}\text{Pb}$ ages in $\text{Ma} \pm 1$ sigma if marked with an asterisk. The circles indicating the SHRIMP analyses are 25 micron in diameter.

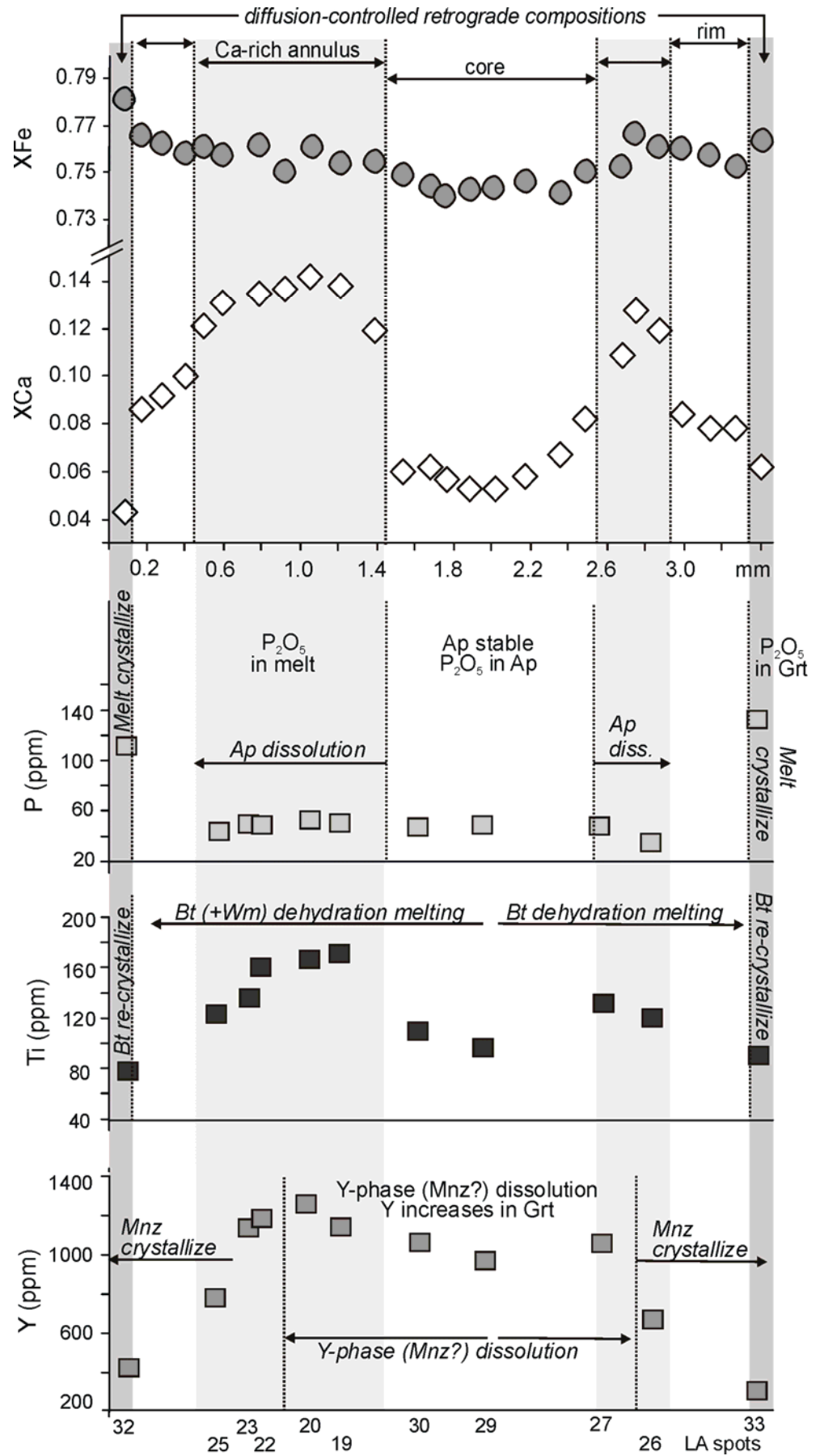


Fig. 4 – Compositional profile of the garnet porphyroblast reported in Fig. 2b. $X_{Ca}=Ca/(Ca+Mg+Fe)$, $X_{Fe}=Fe/(Fe+Mg)$. P, Ti and Y concentrations have been measured using the laser ablation technique; each

point analysis refers to the correspondent numbers in Fig. 2b. The light grey field refers to the Ca-rich annulus, whereas the dark grey field represents the outermost garnet rim characterized by diffusion-controlled retrograde compositions.

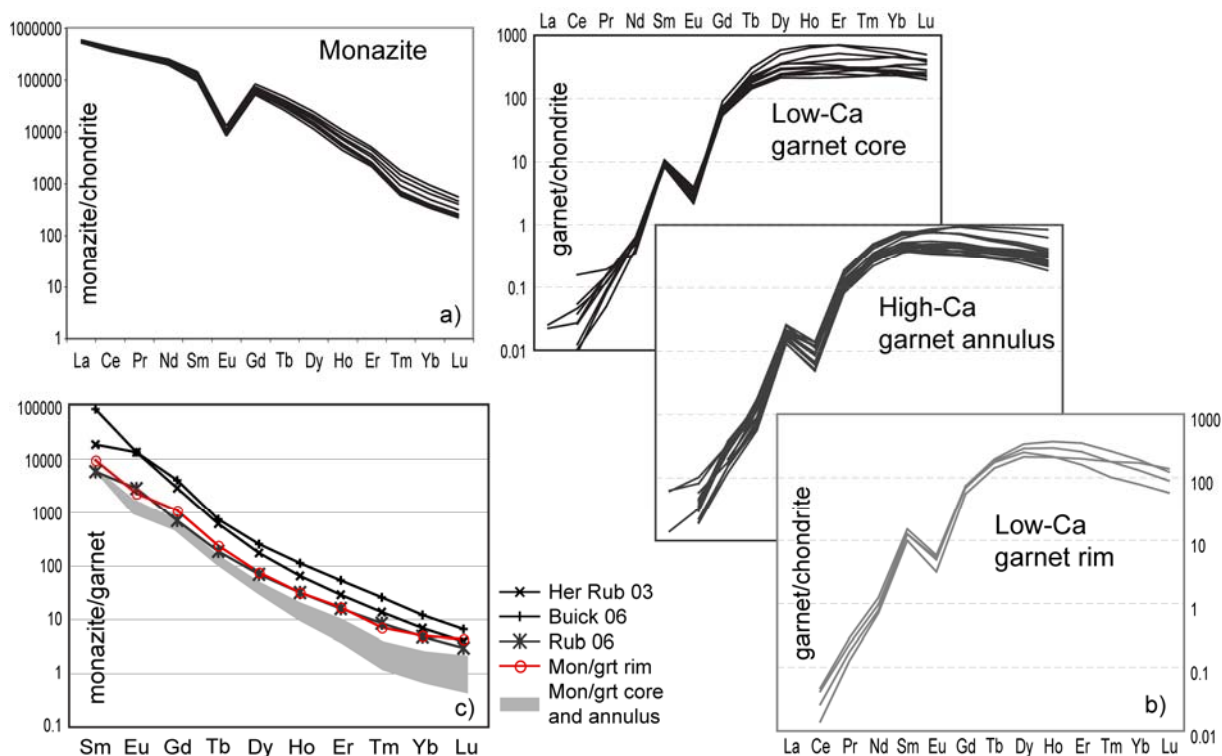


Fig. 5 – (a, b) Chondrite normalised REE patterns for monazite and garnet, respectively. The garnet patterns are indicated by domain. c) REE partitioning between average monazite and different portions of the garnet. The grey area covers the range of partitioning with the garnet low-Ca core and high-Ca annulus, whereas the partitioning with the average garnet rim is represented by the pattern with circles. HerRub 03 = Hermann and Rubatto (2003); Buick 06 = Buick et al. (2006); Rubatto 06 = Rubatto et al. (2006).

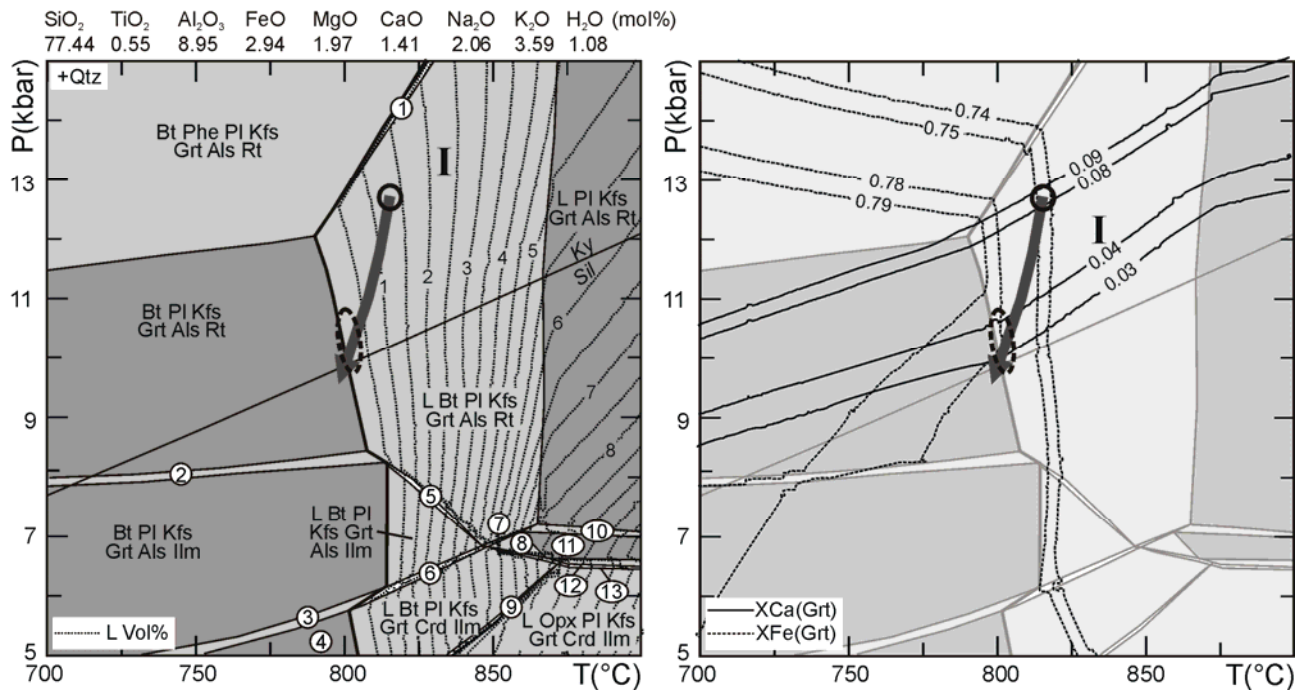


Fig. 6 – (a) P-T pseudosection for sample AR2 in the NKCFMASTH system, calculated using the bulk composition AR2a (Table 1). White, light-, medium- and dark-grey fields are di- tri-, quadri- and quini-variant fields, respectively. The thick line represents the *solidus* of the system. Dotted lines are the melt isomodes (in vol%). Peak assemblage (melt + Grt + Bt + Kfs + Pl + Ky + Qtz + Rt) is shown as field I. Black ellipses constrain the growth of garnet rim (peak P-T conditions: continuous line), and P-T conditions estimated for final melt crystallization (dashed line), as inferred from mineral isomodes and compositional isopleths (see text for discussion). The grey arrow is the P-T path inferred from sample AR2. Numbered fields are: (1) L-Bt-Phe-Pl-Kfs-Grt-Als-Rt; (2) Bt-Pl-Kfs-Grt-Als-Rt-Ilm; (3) Bt-Pl-Kfs-Grt-Crd-Als-Ilm; (4) Bt-Pl-Kfs-Grt-Crd-Ilm; (5) L-Bt-Pl-Kfs-Grt-Als-Rt-Ilm; (6) L-Bt-Pl-Kfs-Grt-Crd-Als-Ilm; (7) L-Bt-Pl-Kfs-Grt-Crd-Als-Rt; (8) L-Bt-Pl-Kfs-Grt-Crd-Rt; (9) L-Opx-Bt-Pl-Kfs-Grt-Crd-Ilm; (10) L-Pl-Kfs-Grt-Crd-Als-Rt; (11) L-Pl-Kfs-Grt-Crd-Als-Rt; (12) L-Opx-Pl-Kfs-Grt-Crd-Rt; (13) L-Opx-Pl-Kfs-Grt-Crd-Rt-Ilm. (b) Compositional isopleths of garnet (X_{Ca} , X_{Fe}) used for the P-T estimates. The entire set of isopleths is available at Fig. A2 as supplementary material. Black ellipses and grey arrow are as in (a).

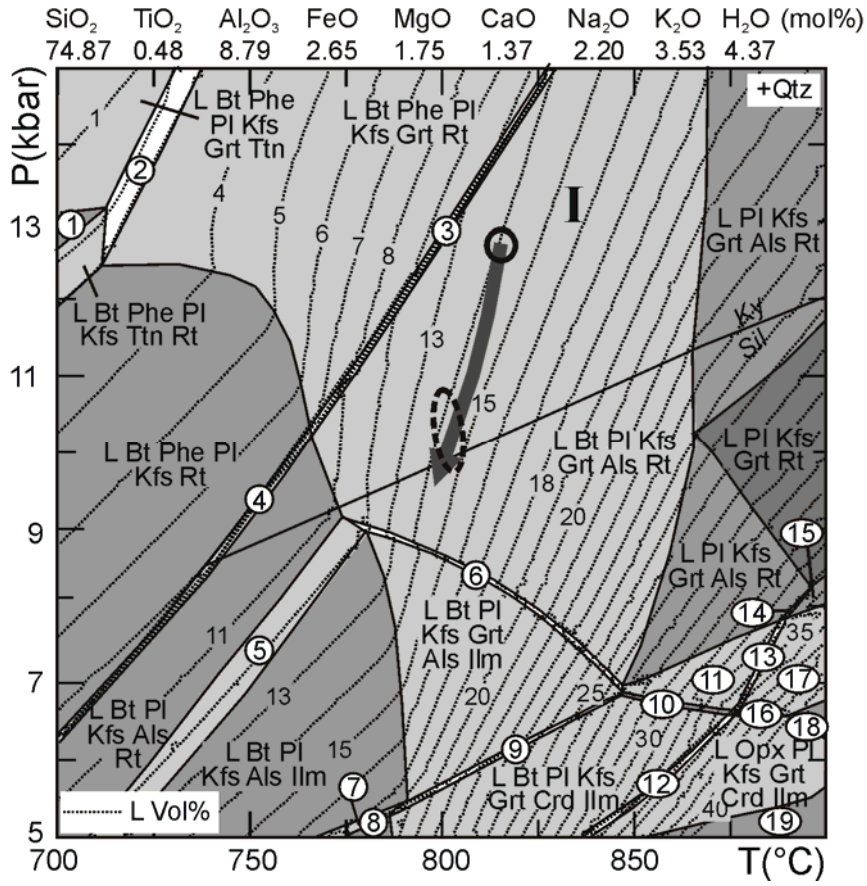


Fig. 7 –P-T pseudosection for sample AR2, calculated using the bulk composition AR2b (Table 1) obtained from re-integration of 14 mol% of melt. The *solidus* of the system is at $T < 670^{\circ}\text{C}$ (not shown in this figure). Black ellipses and grey arrow as in Fig. 6. Numbered fields are: (1) L-Bt-Phe-Pl-Kfs-Rt; (2) L-Bt-Phe-Kfs-Grt-Ttn-Rt; (3) L-Bt-Phe-Pl-Kfs-Grt-Als-Rt; (4) L-Bt-Phe-Pl-Kfs-Als-Rt; (5) L-Bt-Pl-Kfs-Als-Rt-Ilm; (6) L-Bt-Pl-Kfs-Grt-Als-Rt-Ilm; (7) L-Bt-Pl-Kfs-Als-Crd-Ilm; (8) L-Bt-Pl-Kfs-Crd-Ilm; (9) L-Bt-Pl-Kfs-Grt-Crd-Als-Ilm; (10) L-Bt-Pl-Kfs-Grt-Crd-Rt-Ilm; (11) L-Bt-Pl-Kfs-Grt-Crd-Rt; (12) L-Opx-Bt-Pl-Kfs-Grt-Crd-Ilm; (13) L-Opx-Bt-Pl-Kfs-Grt-Rt-Ilm; (14) L-Opx-Pl-Kfs-Grt-Als-Rt; (15) L-Opx-Pl-Kfs-Grt-Rt; (16) L-Opx-Pl-Kfs-Grt-Crd-Rt-Ilm; (17) L-Opx-Pl-Kfs-Grt-Ilm-Rt; (18) L-Opx-Pl-Kfs-Grt-Ilm; (19) L-Opx-Pl-Kfs-Grt-Ilm.

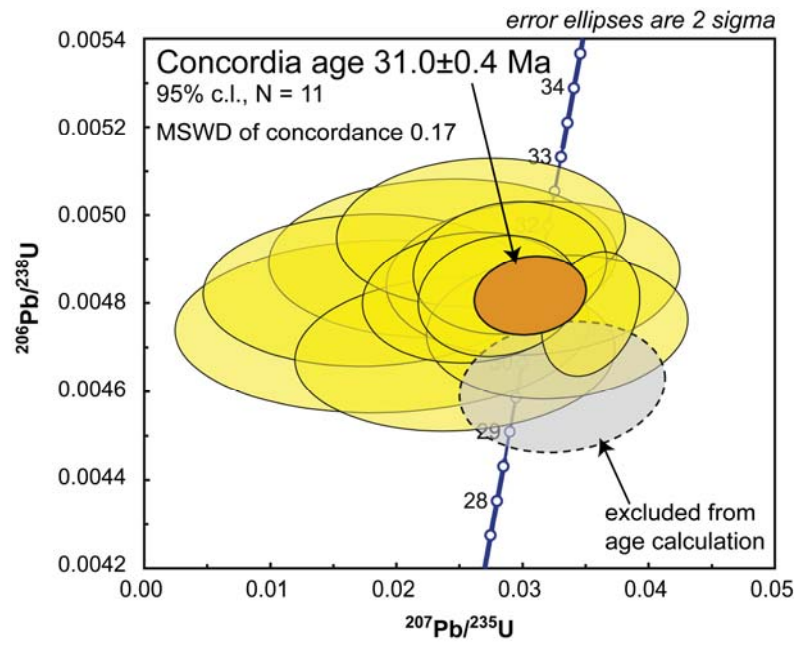


Fig. 8. – Concordia diagram for SHRIMP U-Pb analyses of monazite.

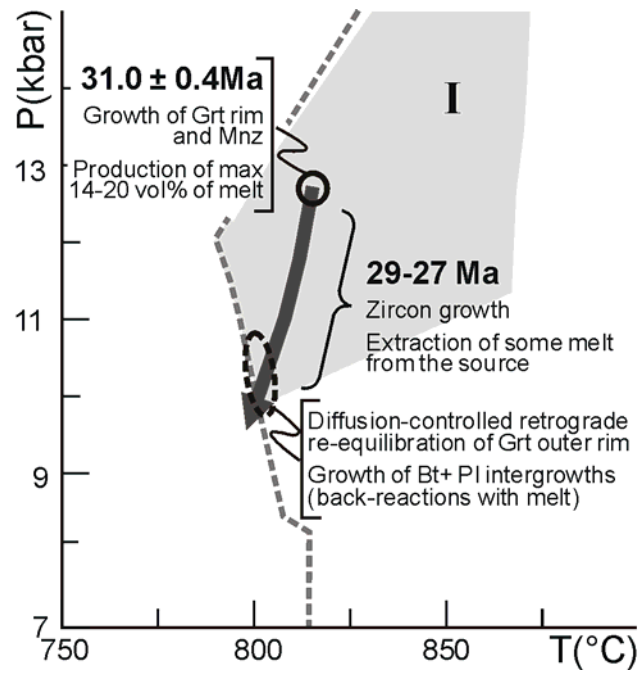


Fig. 9 – P-T-time evolution of sample AR2 as inferred from pseudosection modelling and monazite-zircon geochronology (data from Fig. 6 and 7). The ellipses constrain the growth of garnet rim (peak P-T conditions: continuous line), and P-T conditions estimated for final melt crystallization (dashed line), as in Figs. 6 and 7. Field I is the same as in Fig. 6. See text for discussion.

Table 1. Representative analyses of garnet, plagioclase, K-feldspar and biotite in sample AR2

Analysis	Garnet						Plagioclase			K-feldspar		Biotite			
	core		Ca-rich annulus		rim		coarse	fine	symp	2.9	3.2	matrix		symp	
	4.14	4.17	4.8	4.9	4.26	4.1	2.1	1.6	5.19			2.16	1.9	5.18	6.37
SiO ₂	38.22	38.20	38.43	38.20	38.00	37.35	62.90	62.88	62.34	65.33	64.68	36.25	36.31	36.37	36.41
TiO ₂	0.00	0.00	0.00	0.00	0.00	0.00	0.00	0.00	0.00	0.00	0.00	4.75	4.19	3.94	3.02
Al ₂ O ₃	21.53	21.71	21.19	21.35	21.54	21.08	22.95	23.39	23.82	18.59	19.19	17.90	18.33	19.48	20.00
FeO	31.15	31.04	28.70	29.37	31.13	32.84	0.00	0.00	0.00	0.00	0.00	17.90	17.76	17.38	16.00
MnO	1.42	1.30	1.28	0.92	1.42	1.49	0.00	0.00	0.00	0.00	0.00	0.00	0.00	0.00	0.00
MgO	6.14	5.93	5.35	5.19	5.47	5.32	0.00	0.00	0.00	0.00	0.00	9.68	9.85	10.28	10.17
CaO	2.05	2.05	4.90	5.07	2.25	1.50	4.78	5.09	5.52	0.00	0.00	0.00	0.00	0.00	0.00
Na ₂ O	0.00	0.00	0.00	0.00	0.00	0.00	8.46	8.48	8.57	1.68	0.84	0.00	0.00	0.00	0.00
K ₂ O	0.00	0.00	0.00	0.00	0.00	0.00	0.38	0.00	0.00	14.47	15.46	9.83	10.14	9.64	9.87
Total	100.51	100.22	99.85	100.10	99.81	99.56	99.47	99.85	100.25	100.07	100.17	96.31	96.58	97.09	95.47
Si	2.99	3.00	3.01	3.00	3.00	2.97	2.81	2.80	2.76	3.00	2.98	2.70	2.71	2.68	2.74
Ti	0.00	0.00	0.00	0.00	0.00	0.00	0.00	0.00	0.00	0.00	0.00	0.27	0.24	0.22	0.17
Al	1.99	2.01	1.97	1.98	2.01	1.98	1.21	1.23	1.24	1.01	1.04	1.57	1.61	1.69	1.77
Fe	2.04	2.04	1.89	1.93	2.06	2.19	0.00	0.00	0.00	0.00	0.00	1.12	1.11	1.07	1.01
Mn	0.09	0.09	0.09	0.06	0.09	0.10	0.00	0.00	0.00	0.00	0.00	0.00	0.00	0.00	0.00
Mg	0.72	0.69	0.63	0.61	0.64	0.63	0.00	0.00	0.00	0.00	0.00	1.08	1.10	1.13	1.14
Ca	0.17	0.17	0.41	0.43	0.19	0.13	0.23	0.24	0.26	0.00	0.00	0.00	0.00	0.00	0.00
Na	0.00	0.00	0.00	0.00	0.00	0.00	0.73	0.73	0.74	0.15	0.08	0.00	0.00	0.00	0.00
K	0.00	0.00	0.00	0.00	0.00	0.00	0.02	0.00	0.00	0.85	0.91	0.94	0.97	0.91	0.95
XCa	0.06	0.06	0.14	0.14	0.07	0.04	XAn	0.23	0.25	0.26	XAb	0.15	0.08	XFe	0.51
XFe	0.74	0.75	0.75	0.76	0.76	0.78	XOr	0.02	0.00	0.00				0.50	0.49

Table 2. Bulk compositions (wt%) used for the modelling

(A)	AR2a	AR2b	melt (14 mol%) 820°C, 14 kbar	AR2 ICP analysis
SiO ₂	71.97	71.19	64.36	72.75
TiO ₂	0.68	0.61	0.00	0.58
Al ₂ O ₃	14.12	14.18	14.78	12.93
FeO	3.27	3.01	0.75	3.75
MgO	1.23	1.12	0.14	1.50
CaO	1.22	1.21	1.12	1.22
Na ₂ O	1.98	2.16	3.77	2.25
K ₂ O	5.23	5.27	5.56	4.41
H ₂ O	0.30	1.25	9.52	0.61
	100.00	100.00	100.00	100.00

AR2a = bulk composition obtained from modal proportions and mineral compositions

AR2b = AR2a + melt reintegrated

(B) Comparison between mode (vol%)
of minerals measured and modelled
at the *solidus*

	measured	modelled at the <i>solidus</i>
Biotite	8.9	7.9
Garnet	3.3	3.2
Kyanite	1.8	1.5
Quartz	38.2	37.5
K-feldspar	28.7	34.3
Plagioclase	19.1	15.5

Table 3. SHRIMP U-Pb analyses of monazite.

Label	UO ₂ wt%	ThO ₂ wt%	Th/U	%Pb com	²⁰⁶ Pb/ ²³⁸ U Age (Ma)	1 sigma absolute	²⁰⁸ Pb/ ²³² Th Age (Ma)	1 sigma absolute	²⁰⁷ Pb/ ²³⁵ U	1 sigma %	²⁰⁶ Pb/ ²³⁸ U	1 sigma %	error correlation
AR2-3	1.0	11.7	11.7	0.00	29.7	0.4	27.43	0.56	0.03317	10.1	0.0046	1.3	0.129
AR2-2	0.9	7.5	8.6	1.63	30.1	0.5	29.21	0.68	0.02459	21.2	0.0047	1.5	0.071
AR2-9	1.3	8.4	6.3	0.27	30.5	0.4	31.31	1.23	0.03274	13.0	0.0047	1.4	0.107
AR2-12	1.0	7.2	7.3	2.54	30.6	0.5	29.75	0.76	0.01882	35.9	0.0048	1.7	0.047
AR2-11	0.9	7.1	7.8	0.00	30.7	0.4	31.84	0.74	0.03542	4.5	0.0048	1.2	0.266
AR2-5	1.2	8.9	7.4	1.35	31.0	0.4	30.39	0.72	0.02581	13.6	0.0048	1.2	0.092
AR2-6	1.4	9.9	7.0	0.94	31.0	0.4	30.48	0.63	0.02806	9.3	0.0048	1.2	0.124
AR2-8	1.3	9.5	7.3	2.35	31.1	0.4	29.80	0.74	0.01767	30.4	0.0048	1.4	0.048
AR2-4	1.1	8.9	7.9	0.58	31.3	0.5	31.54	0.70	0.03081	15.5	0.0049	1.5	0.094
AR2-1	1.1	9.1	8.4	0.85	31.4	0.4	30.97	0.63	0.02898	10.8	0.0049	1.3	0.115
AR2-7	1.2	9.0	7.2	1.69	31.5	0.5	31.28	0.72	0.02362	24.0	0.0049	1.5	0.062
AR2-10	1.0	7.0	6.9	1.19	31.9	0.4	30.28	0.71	0.02665	17.6	0.0050	1.4	0.079

%Pb com = percent of common Pb

Table 4. SHRIMP U-Pb analyses of zircon.

Label	U (ppm)	Th (ppm)	Th/U	%Pb com	²⁰⁶ Pb/ ²³⁸ U Age (Ma)	1 sigma absolute	²⁰⁷ Pb/ ²⁰⁶ Pb Age (Ma)	1 sigma absolute	Discordance %	²⁰⁷ Pb/ ²³⁵ U	1 sigma %	²⁰⁶ Pb/ ²³⁸ U	1 sigma %	error correlation
AR2-22.1	943	19	0.020	0.88	20.4	0.3				0.01661	16.7	0.003162	1.35	0.08
AR2-16.1	2942	37	0.013	0.14	27.5	0.3				0.02682	3.1	0.004272	1.10	0.36
AR2-4.2	1909	24	0.013	0.03	28.0	0.3				0.02815	5.1	0.004351	1.06	0.21
AR2-21.1	5625	89	0.016	0.32	27.6	0.4				0.02889	2.8	0.004286	1.17	0.41
AR2-20.1	4793	32	0.007	0.20	28.4	0.3				0.02922	2.2	0.004412	0.99	0.45
AR2-15.1	4241	64	0.015	0.31	28.9	0.3				0.02802	3.4	0.004500	1.07	0.32
AR2-18.1	4370	32	0.007	0.23	29.2	0.3				0.02947	3.0	0.004540	1.04	0.35
AR2-19.1	7137	54	0.008	0.26	28.0	0.3				0.03070	1.9	0.004351	1.05	0.55
AR2-12.1	8878	65	0.007	0.12	27.1	0.3				0.03358	1.6	0.004223	1.03	0.63
AR2-5.1	709	52	0.073	0.04	426	5	494	22	16	0.53723	1.5	0.068270	1.13	0.75
AR2-25.1	2031	18	0.009	0.01	430	5	488	23	14	0.54119	1.5	0.068963	1.12	0.74
AR2-23.1	2722	15	0.006	0.02	442	4	449	14	2	0.54708	1.2	0.070972	1.00	0.84
AR2-6.1	772	44	0.058	0.01	443	5	438	18	-1	0.54534	1.4	0.071100	1.13	0.82
AR2-24.1	1885	20	0.011	0.02	444	4	448	14	1	0.54916	1.2	0.071277	1.02	0.85
AR2-7.1	453	62	0.137	0.02	449	4	425	26	-5	0.55040	1.5	0.072152	1.01	0.66
AR2-29.1	321	20	0.062	0.07	463	5	432	40	-7	0.56978	2.1	0.074465	1.04	0.50
AR2-14.1	3435	7	0.002	0.04	467	5	433	9	-7	0.57550	1.2	0.075177	1.09	0.94
AR2-30.1	305	55	0.180	0.30	467	5	368	48	-21	0.55926	2.4	0.075204	1.06	0.44
AR2-2.1	240	236	0.982	0.34	475	5	302	47	-36	0.55175	2.3	0.076407	1.07	0.46
AR2-23.2	737	202	0.273	0.06	622	6	611	14	-2	0.84143	1.2	0.101364	1.07	0.86
AR2-17.1	551	344	0.625	0.05	682	6	677	16	-1	0.95530	1.2	0.111603	0.99	0.80
AR2-3.1	720	133	0.184	0.02	775	10	899	41	16	1.21581	2.4	0.127759	1.31	0.55
AR2-1.1	544	212	0.389	0.11	866	12	927	15	7	1.38759	1.6	0.143847	1.47	0.90
AR2-1.1B	477	189	0.397	0.01	876	18	951	18	9	1.41959	2.4	0.145470	2.24	0.93
AR2-4.1	1046	85	0.082	0.03	895	9	1149	13	28	1.60356	1.2	0.148929	1.07	0.86
AR2-28.1	968	90	0.093	0.05	915	9	895	12	-2	1.44844	1.3	0.152551	1.10	0.88
AR2-8.1	374	96	0.256	0.05	978	9	964	14	-1	1.60843	1.2	0.163805	1.00	0.82
AR2-9.1	219	111	0.506	0.00	983	13	1019	21	4	1.66245	1.8	0.164795	1.44	0.81
AR2-26.1	200	66	0.330	0.13	999	12	988	19	-1	1.66467	1.6	0.167550	1.34	0.83
AR2-20.2	141	113	0.800	0.15	1349	13	1598	15	18	3.16309	1.3	0.232699	1.09	0.81
AR2-10.1	137	47	0.340	0.09	1589	19	1629	31	3	3.86503	2.1	0.279517	1.33	0.62

%Pb com = percent of common Pb

Table A. Mineral trace element composition. Concentrations are given in ppm, unless otherwise indicated.

	Ca (wt%)	P	Ti	Rb	Sr	Y	Zr	La	Ce	Pr	Nd	Sm	Eu	Gd	Tb	Dy	Ho	Er	Tm	Yb	Lu	Hf	Ta	Th	U
Garnet core																									
AR2-grt13	1.4	86	94	0.13	0.17	303	2.4	<0.010	0.033	0.014	0.26	1.4	0.17	10	5.0	51	11	34	5.5	41	6.2	0.26	0.04	<0.015	0.431
AR2-grt12	1.6	46	96	0.14	0.06	388	2.0	<0.010	0.033	<0.005	0.18	1.3	0.14	11	5.2	59	15	46	6.6	40	5.4	0.25	0.06	<0.015	<0.015
AR2-grt18	1.8	70	94	0.12	0.05	345	2.4	0.005	0.016	0.014	0.28	1.5	0.22	12	5.7	58	13	39	5.6	37	4.9	0.20	0.05	<0.015	<0.015
AR2-grt15	1.6	57	93	0.14	0.06	461	2.5	<0.010	0.023	0.014	0.22	1.2	0.12	12	6.3	69	16	49	7.5	51	6.8	0.26	0.06	<0.015	0.019
AR2-grt11	2.0	52	121	0.14	0.05	476	2.9	<0.010	0.016	0.011	0.22	1.4	0.19	13	6.7	72	17	49	6.9	44	5.7	0.29	0.06	<0.015	<0.015
AR2-grt14	1.9	39	64	0.19	0.11	604	2.8	<0.010	0.095	0.017	0.16	1.3	0.17	14	7.5	84	20	64	10.2	73	10	0.36	0.07	<0.015	0.035
AR2-grt16	2.1	50	116	0.20	0.09	627	2.3	<0.010	<0.007	<0.005	0.26	1.4	0.18	13	6.9	87	24	81	11.5	71	10	0.30	0.11	<0.015	<0.015
AR2-grt35	1.6	39	96	0.13	0.11	352	2.0	0.006	0.027	0.011	0.23	1.2	0.15	11	5.4	56	13	42	7.0	53	8.4	0.19	0.05	0.005	0.016
AR2-grt28	2.0	93	91	0.12	0.05	543	2.6	<0.005	0.007	0.008	0.25	1.5	0.20	15	7.9	86	19	52	6.7	39	4.8	0.32	0.06	0.004	0.008
AR2-grt29	1.9	48	95	0.26	0.09	968	2.4	<0.005	0.006	0.004	0.19	1.3	0.13	14	8.7	120	34	110	15.7	94	12	0.37	0.12	<0.004	<0.005
AR2-grt30	2.2	47	109	0.26	0.07	1062	2.4	<0.005	0.005	0.007	0.24	1.5	0.17	18	10.8	141	37	109	14.1	79	9.2	0.45	0.13	0.005	0.008
Garnet rim																									
AR2-grt24	2.7	106	77	0.12	0.03	516	2.7	<0.005	0.028	0.026	0.55	2.2	0.32	14	6.9	80	20	55	6.3	30	3.0	0.31	0.07	<0.004	0.012
AR2-grt32	2.4	111	77	0.08	0.02	416	2.2	<0.005	0.025	0.021	0.44	1.8	0.29	13	6.4	69	16	40	4.3	20	2.1	0.26	0.05	<0.004	0.017
AR2-grt33	2.2	132	90	0.05	0.02	306	2.9	<0.005	0.016	0.016	0.35	1.8	0.27	14	6.2	60	11	25	2.4	12	1.4	0.23	0.04	<0.004	0.009
AR2-grt31	1.7	204	84	0.08	0.03	306	4.3	<0.005	0.008	0.011	0.32	1.4	0.17	11	5.0	51	11	31	4.3	27	3.3	0.22	0.04	<0.004	0.006
Garnet annulus																									
AR2-grt9	2.6	62	101	0.18	0.13	591	2.3	<0.010	0.013	0.014	0.36	1.9	0.28	16	7.9	87	22	69	10.0	62	7.6	0.27	0.08	<0.015	<0.015
AR2-grt17	2.9	49	126	0.19	0.09	678	2.6	<0.010	0.012	0.014	0.28	1.9	0.27	17	9.0	102	25	72	9.2	53	6.6	0.46	0.09	<0.015	<0.015
AR2-grt10	3.1	48	132	0.21	0.09	699	3.2	<0.010	0.011	0.011	0.25	1.9	0.29	19	9.5	105	25	76	10.5	64	8.3	0.35	0.10	<0.015	0.020
AR2-grt4	3.5	48	133	0.22	0.06	707	3.0	<0.010	<0.007	0.014	0.30	2.1	0.35	21	10.3	112	27	77	9.8	56	7.2	0.39	0.11	<0.015	<0.015
AR2-grt1	3.6	50	123	0.21	0.07	702	2.7	<0.010	<0.007	0.016	0.31	2.2	0.34	21	10.8	114	26	70	8.9	49	6.1	0.39	0.10	<0.015	<0.015
AR2-grt2	3.7	131	124	0.26	0.14	804	2.9	0.014	0.062	0.030	0.40	2.2	0.37	21	11.5	127	30	82	10.4	58	7.3	0.43	0.11	0.014	1.031
AR2-grt8	3.7	44	144	0.15	0.07	599	3.1	<0.010	<0.007	0.018	0.41	2.4	0.36	22	9.7	95	21	59	7.6	44	5.2	0.30	0.08	<0.015	<0.015
AR2-grt3	3.8	51	125	0.19	0.10	665	2.9	<0.010	0.035	0.016	0.52	2.3	0.37	21	10.2	106	24	67	8.5	48	5.9	0.47	0.09	<0.015	0.034
AR2-grt7	4.1	49	152	0.14	0.12	566	3.5	<0.010	0.026	0.023	0.54	2.7	0.48	25	10.4	92	18	52	7.1	44	5.6	0.32	0.05	<0.015	<0.015
AR2-grt6	4.3	54	150	0.15	0.06	603	3.7	<0.010	0.018	0.031	0.68	2.9	0.50	24	10.4	95	20	54	7.3	44	5.3	0.32	0.09	<0.015	0.015
AR2-grt5	4.4	53	151	0.17	0.06	608	4.2	<0.010	0.024	0.035	0.62	2.7	0.52	24	9.7	93	21	61	8.5	51	6.4	0.41	0.09	<0.015	<0.015
AR2-grt26	4.2	33	120	0.13	0.04	662	2.2	<0.010	0.028	0.026	0.64	2.8	0.52	23	10.7	107	23	59	7.2	39	4.5	0.35	0.08	<0.015	0.015
AR2-grt34	4.4	60	153	0.21	0.24	660	4.0	0.015	0.049	0.032	0.64	2.8	0.50	22	9.7	98	24	73	10.0	60	8.0	0.34	0.09	<0.015	0.106
AR2-grt25	4.4	42	121	0.17	0.05	790	2.3	<0.010	0.019	0.028	0.61	2.6	0.47	27	12.3	123	26	68	8.6	49	5.6	0.40	0.09	<0.015	<0.015
AR2-grt23	4.4	49	135	0.27	0.08	1136	3.4	<0.010	0.021	0.024	0.79	3.6	0.62	30	14.7	166	40	115	14.6	83	10	0.56	0.14	<0.015	0.019
AR2-grt22	4.9	48	160	0.26	0.07	1180	5.2	<0.010	0.022	0.023	0.58	3.1	0.76	35	16.4	179	41	112	13.9	77	9.2	0.61	0.15	<0.015	<0.015
AR2-grt20	5.0	51	165	0.34	0.11	1252	5.7	<0.010	0.018	0.026	0.62	2.9	0.68	31	15.0	173	46	146	20.2	118	15	0.62	0.16	<0.015	<0.015
AR2-grt19	5.0	49	171	0.38	0.12	1124	5.5	<0.010	0.020	0.025	0.60	2.8	0.66	26	12.5	148	43	151	22.3	141	20	0.51	0.14	<0.015	<0.015
AR2-grt21	5.3	52	148	0.25	0.07	1217	5.1	<0.005	0.028	0.027	0.58	3.7	0.77	37	17.6	188	42	112	13.6	75	8.7	0.55	0.17	<0.004	<0.005
Monazite																									
AR2-m3	1.7	n.a	239	n.a.	n.a.	7186	2.2	126043	220869	24766	92228	15634	546	11879	1123	3423	291	376	15	57	5.9	9.0	1.0	105973	9160
AR2-m1	1.5	n.a	237	n.a.	n.a.	5996	2.3	136644	229649	24573	87951	13931	471	10147	920	2755	242	338	14	55	5.3	7.3	0.8	84311	8959
AR2-m4	1.4	n.a	243	n.a.	n.a.	6780	2.3	131382	233459	26061	95509	16007	516	11629	1086	3257	280	371	15	57	5.7	8.6	1.0	79150	8428
AR2-m6	1.5	n.a	252	n.a.	n.a.	9238	2.4	129779	236949	26821	100925	17548	566	13385	1306	4219	382	507	23	81	7.7	11.0	1.3	83626	10429
AR2-m7	1.3	n.a	226	n.a.	n.a.	6972	2.2	121069	218901	24556	90946	15408	502	11242	1063	3273	289	388	17	61	5.9	8.5	1.0	71295	9049
AR2-m8	1.5	n.a	279	n.a.	n.a.	10327	2.6	137458	253729	29014	108970	19209	625	14542	1435	4646	429	589	29	105	9.7	12.0	1.5	85873	10933
AR2-m9	1.5	n.a	271	n.a.	n.a.	13639	2.6	140379	260392	29973	113800	20800	715	16440	1684	5883	574	811	43	150	14	15.0	2.0	78922	10136
AR2-m10	1.3	n.a	239	n.a.	n.a.	7690	2.3	126670	233021	26332	97641	16940	558	12443	1193	3701	321	417	17	64	6.4	9.6	1.1	68694	8786
AR2-m11	1.2	n.a	246	n.a.	n.a.	11100	2.4	132298	238745	27031	102720	18088	551	14064	1428	5006	493	697	36	125	11	12.8	1.7	65765	7679

n.a = not analysed

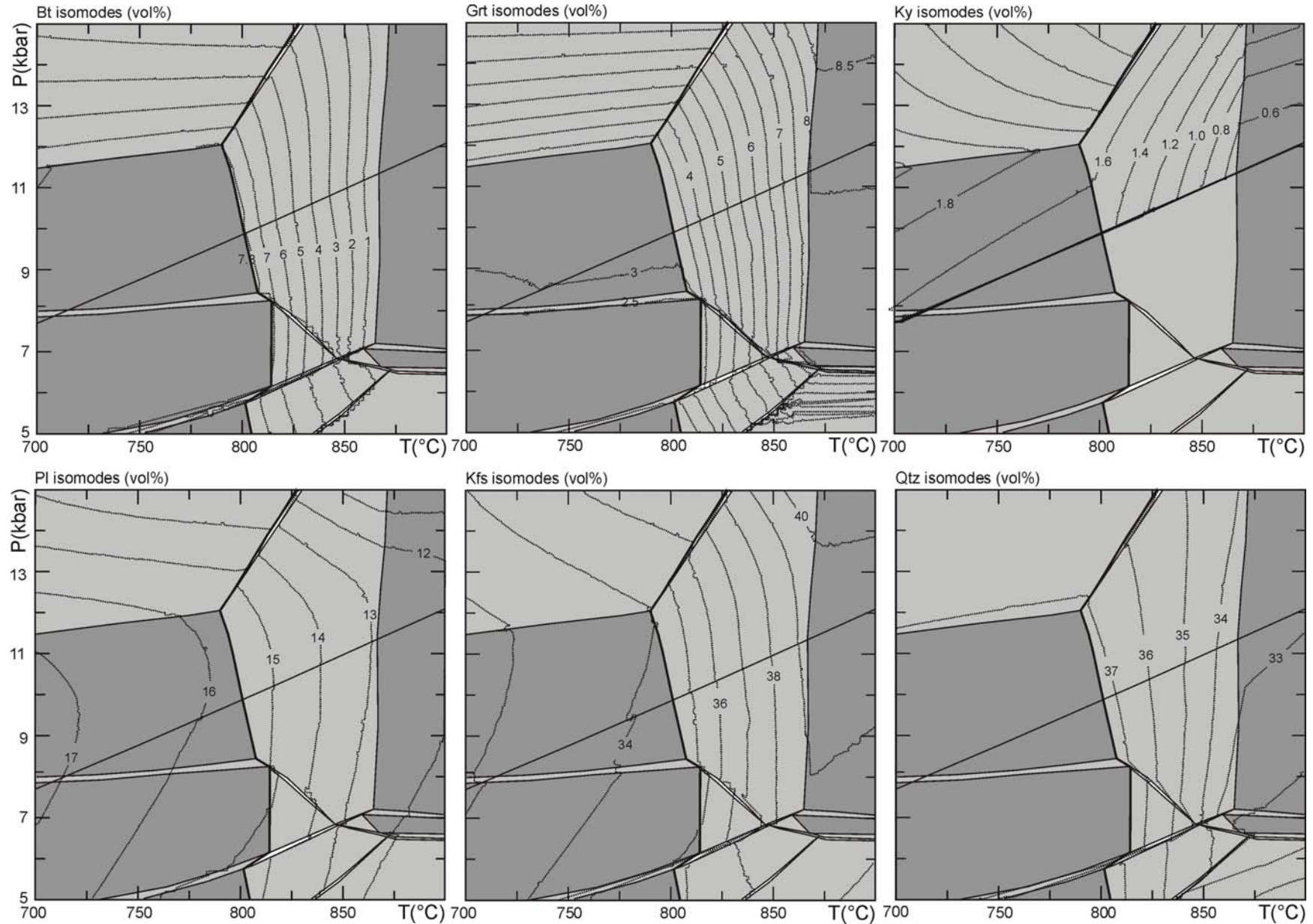


Fig. A1 – P-T pseudosection for sample AR2, calculated using the bulk composition AR2a (see Fig. 6 for details), with isomodes (in vol%) of biotite, garnet, kyanite, plagioclase, K-feldspar and quartz. The thick line represents the *solidus* of the system.

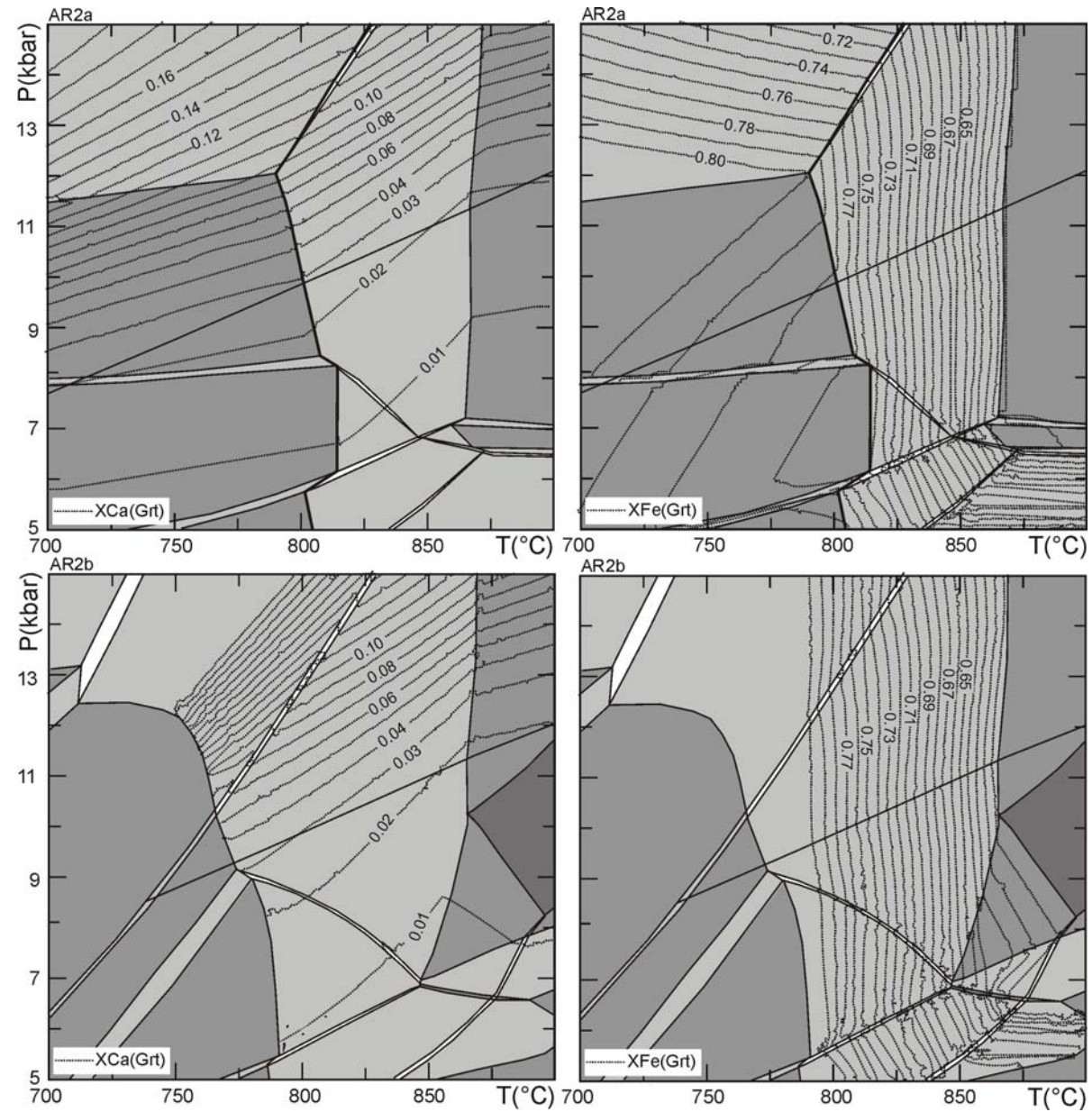


Fig. A2 – P-T pseudosections for sample AR2, calculated using the bulk compositions AR2a and AR2b (see Table 2a, Fig. 6 and 7 for details), with compositional isopleths of garnet (X_{Ca} and X_{Fe}).